ELECTRONIC AND PHONONIC CONTRIBUTIONS TO NEAR-INFRARED REFLECTIVITY OF OXIDE PIGMENTS

Worasarit Saengsui

A Thesis submitted in Partial Fulfillment of the Requirements for the

Degree of Doctor of Philosophy in Physics

Suranaree University of Technology

Academic Year 2019

บทบาทของอิเล็กตรอนและโฟนอนต่อการสะท้อนรังสีอินฟราเรดใกล้ของผงสีออกไซด์

นายวรสฤษดิ์ แสงสุย

วิทยานิพนธ์นี้เป็นส่วนหนึ่งของการศึกษาตามหลักสูตรปริญญาวิทยาศาสตรดุษฎีบัณฑิต
สาขาวิชาฟิสิกส์
มหาวิทยาลัยเทคโนโลยีสุรนารี
ปีการศึกษา 2562

ELECTRONIC AND PHONONIC CONTRIBUTIONS TO NEAR-INFRARED REFLECTIVITY OF OXIDE PIGMENTS

Suranaree University of Technology has approved this thesis submitted in partial fulfillment of the requirements for the Degree of Doctor of Philosophy.

Thesis Examining Committee

(Assoc. Prof. Dr. Panomsak Meemon)
Chairperson

(Assoc. Prof. Dr. Worawat Meevasana)
Member (Thesis Advisor)

(Asst. Prof. Dr. Michael F. Smith)
Member

Narong Chanlek
(Dr. Narong Chanlek)
Member (Thesis Co-advisor)

S. Supothina
(Dr. Sitthisuntorn Supothina)
Member

Chatchai Jothit
(Assoc. Prof. Dr. Chatchai Jothityangkoon)
Vice Rector for Academic Affairs
and Quality Assurance

(Prof. Dr. Santi Maensiri)
Dean of Institute of Science

วรสฤษดิ์ แสงสุย : บทบาทของอิเล็กตรอนและโฟนอนต่อการสะท้อนรังสีอินฟราเรดใกล้ของผงสีออกไซด์ (ELECTRONIC AND PHONONIC CONTRIBUTIONS TO NEAR-INFRARED REFLECTIVITY OF OXIDE PIGMENTS). อาจารย์ที่ปรึกษา : รองศาสตราจารย์ ดร.วรวัฒน์ มีวาสนา, 78 หน้า.

ผงสีออกไซด์ การดูดกลืนโดยอิเล็กตรอน การดูดกลืนโดยแลตทิซ การสะท้อนรังสีอินฟราเรดใกล้

ในการศึกษานี้ได้ทำการเตรียมผงสีเซรามิกส์จำนวนสี่อนุกรมโดยวิธีปฏิกิริยาในสถานะของแข็ง และศึกษาโครงสร้างผลึก สมบัติการสะท้อนรังสีอินฟราเรดใกล้ โครงสร้างอิเล็กตรอน และสมบัติการสั่นของแลตทิซของผงสี จากผลการทดลองข้างต้นทำให้สามารถหาค่าสหสัมพันธ์ระหว่างสมบัติการดูดกลืนโดยอิเล็กตรอนหรือโฟนอนและการสะท้อนรังสีอินฟราเรดใกล้ของผงสี โดยสมมติฐานในการทดลองนี้คือ ค่าสหสัมพันธ์ระหว่างตำแหน่งสูงสุดของแถบพลังงานเวเลนซ์ที่ได้จากการวิเคราะห์สเปกตรัมโฟอิมิสชันและการสะท้อนรังสีอินฟราเรดควรมีค่าในทางบวกอย่างมีนัยสำคัญ ในขณะที่ค่าสหสัมพันธ์ระหว่างพื้นที่ใต้สัญญาณรามานที่ได้จากการวิเคราะห์สเปกตรัมรามานและการสะท้อนรังสีอินฟราเรดควรมีค่าในทางลบอย่างมีนัยสำคัญ ผลการทดลองแสดงให้เห็นว่าผงสีออกไซด์จำนวนสามอนุกรมแสดงค่าสหสัมพันธ์ระหว่างปริมาณดังกล่าวเป็นไปตามที่คาดการณ์ไว้ ยกเว้นผงสีชุด $Cr_xSb_xTi_{1-2x}O_2$ ผลการทดลองแสดงให้เห็นถึงการวิเคราะห์การเปลี่ยนแปลงค่าการสะท้อนรังสีอินฟราเรดใกล้จากการเจือโครงสร้างสารประกอบเซรามิกส์และชี้ให้เห็นถึงบทบาทของอิเล็กตรอนและโฟนอนต่อสมบัติทางการภาพต่าง ๆ ของสารประกอบออกไซด์

สาขาวิชาฟิสิกส์ ลายมือชื่อนักศึกษา Worasarit

ปีการศึกษา 2562 ลายมือชื่ออาจารย์ที่ปรึกษา

WORASARIT SAENGSUI : ELECTRONIC AND PHONONIC CONTRIBUTIONS TO NEAR-INFRARED REFLECTIVITY OF OXIDE PIGMENTS. THESIS ADVISOR : ASSOC. PROF. WORAWAT MEEVASANA, Ph.D. 78 PP.

OXIDE PIGMENT, ELECTRONIC ABSORPTION, LATTICE ABSORPTION, NEAR-INFRARED REFLECTIVITY

Four ceramic pigment series were prepared by solid state reaction method and the crystal structure, near-infrared reflectance, occupied electronic state, and lattice vibration spectrum of all samples were studied. The correlations between electronic/phononic (lattice) properties and near-infrared reflectance in all series were investigated. The positive correlation between valence band maximum position extracted from photoemission spectroscopy measurements and near-infrared reflectance are anticipated while the negative correlation between integrated Raman signal area obtained from Raman spectra are expected. The results show that three out of four oxide pigment series exhibit the correlation behavior as proposed except the $Cr_xSb_xTi_{1-2x}O_2$. The results pave the way for a simple evaluation of near-infrared reflectance change due to doping or substitution in ceramics pigments and hint a scheme on contribution of electron and phonon to other physical properties of oxide materials.

School of Physics	Student's signature Worasarit
Academic Year 2019	Advisor's signature

ACKNOWLEDGEMENTS

My thesis could not have been completed without many great help and support from many people. First, I would like to thank my advisor, Assoc. Prof. Dr. Worawat Meevasana. I appreciate his support and encouragement in research works and life skills.

I would like to thank Dr. Sitthisuntorn Supothina, Nuchjarin Sangwong, and Mantana Suwan from MTEC, NSTDA, as well as Asst. Prof. Dr. Pattana Rakkwamsuk, Chalita Tangon, and Teerasak Tangkittimasak from KMUTT for kindly provide pigment samples, near-infrared reflectance, and structural information. Without this help, the outcome of this study could not be achieved.

In addition, I would like to thank all the members of Meevasana group for always supporting.

Finally, I would like to acknowledge the financial support from graduate scholarship by Synchrotron Light Research Institute (SLRI). This work has been partially supported by Suranaree University of Technology and the Research Network NANOTEC (RNN) program of the National Nanotechnology Center (NANOTEC), NSTDA.

Worasarit Saengsui

CONTENTS

Page

CHAPTER

CONTENTS (Continued)

LIST OF FIGURES

LIST OF FIGURES (Continued)

Figure **Page**

LIST OF FIGURES (Continued)

Figure **Page**

LIST OF FIGURES (Continued)

LIST OF FIGURES (Continued)

LIST OF FIGURES (Continued)

LIST OF TABLES

Table **Page**

CHAPTER I

INTRODUCTION

In the past decades, increasing demand for electrical usage, decreasing of natural resources, and emerging global warming, have aroused the attention of the human. Energy consumption in building is the main part in the process of city operation. Hence, the development of new materials for energy saving will most likely become an important topic in the next decades (Santamouris *et al.*, 2011). Cool materials with high solar reflectance have become the main concern for material scientists to save natural resources, alleviate the urban heat island effect and decelerate global warming (Takebayashi and Moriyama, 2007).

Solar heating is directly a consequence of near-infrared radiation (700-2500 nm) from sun (Kaur *et al.*, 2012). Hence, highly near-infrared (NIR) reflective materials for painting and roofing can effectively prevents the heat penetration into building which in turn reduces the temperature of the building (Raj *et al.*, 2017). As a result, coating the building and roof using NIR reflective pigment could minimize the heat accumulation in building leading to a significantly decreasing of energy consumption (Jansen and Letschert, 2000).

Currently, the main approach for the development of oxide NIR-reflective pigments is the substitution of the elements in based pigment structure by the potential elements. However, there is no general rule guiding the NIR-reflective pigment developer for the elemental choice and substitution level.

In this work, electronic and phononic absorption properties of different set of pigments have been studied using x-ray photoemission spectroscopy and Raman spectroscopy respectively and the correlation of these properties with near-infrared reflectance in several oxide pigments has been investigated and analyzed systematically. The electronic and phononic absorption behaviors of pigment has been used to determine the role of electron and phonon on near-infrared reflectance of oxide pigments. The result has then been used to generalize the strategy for the improvement of near infrared reflectance in oxide pigment.

Research objective / Purposes of the study

- To evaluate the contribution of electronic and phononic absorption to the near infrared reflectance in oxide pigments.
- To provide the general doping/substitution criteria for the improvement of near infrared reflectance in oxide pigments.
- To comprehend knowledge on the physics of absorption in metal oxide material.

CHAPTER II

LITERATURE REVIEW

2.1 Solar radiation and near-infrared reflective pigment

All ordinary matter emits electromagnetic radiation, called thermal radiation, when its temperature is above absolute zero which is a conversion of internal energy into electromagnetic energy. By contrast, all ordinary matter absorbs electromagnetic radiation to an extent. In thermodynamic equilibrium, a black body, an object that absorbs all frequencies of the incident radiation, emits electromagnetic radiation called black-body radiation, with a characteristic temperature-dependent wavelength distribution.

Extraterrestrial solar irradiation can be considered as a black body radiation with some distortion from ideal curve. The solar radiation at sea level, shown in figure 2.1, exhibit the drop of overall intensity with many glitches due to the absorption by atmospheric species, *i.e.*, water molecule, ozone, carbon dioxide and oxygen molecule. Electromagnetic radiation from sun mainly consists of ultraviolet, visible and near-infrared radiation. Almost half of solar radiation at sea level lied in near infrared regime (700-2500 nm) as shown in figure 2.1.

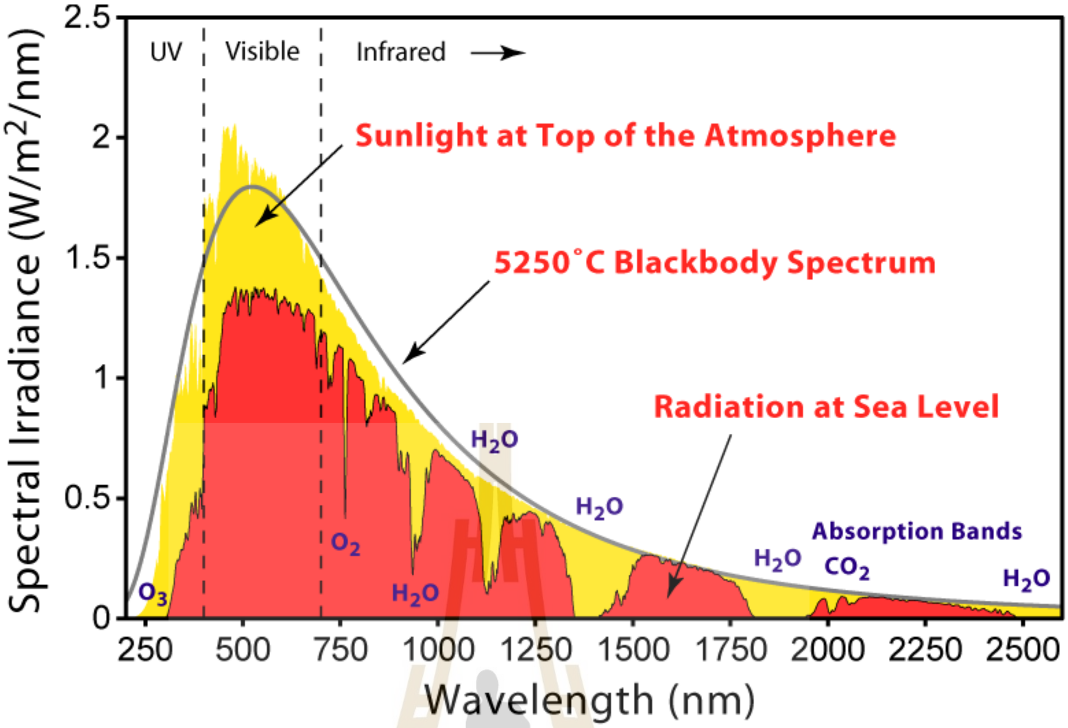

Figure 2.1 Solar radiation spectrum showing the distribution of radiation in three regions, *i.e.*, ultraviolet, visible and near infrared.

(Source: https://en.wikipedia.org/wiki/Air_mass_(solar_energy)).

Radiant barrier is a class of material that can reflect thermal radiation and diminish the heat penetration. Near-infrared reflective pigment is considered to be radiant barrier that block the heat transfer into building. From the fact that heat accumulation from solar radiation results from near-infrared absorption (Malshe and Bendiganavale, 2008), it follows that coverage of the walls and roof with NIR reflective materials could effectively mitigate the penetration of heat from solar radiation into the building (Baneshi *et al*., 2016).

The use of highly near-infrared reflective coatings helps maintain lower exterior surface temperatures of building and consequently contributes to increased indoor thermal comfort during the hot season, which reduces the need for cooling.

This technique for improving thermal comfort inside buildings (Santamouris *et al*., 2007) is low cost, effective, easy to apply, energy efficient and helps reduce the phenomenon of urban heat island (Synnefa *et al*., 2007). The necessity for cool non-white products arose because heat-absorbing darker colors, which are often preferred for aesthetic reasons, contribute to urban heat island and because they serve as a glare control remedy for avoiding “white blight”. This led to the development of cool paints of darker colors, but such special pigment still reflected solar radiation (Synnefa *et al*., 2007). Studies by Akbari *et al*. in 2005 showed that raising the solar reflectance of a roof from 0.1–0.2 to 0.6 can reduce the amount of energy needed to cool a building by more than 20%.

Near-infrared absorption spectroscopy is main tool used to quantify the ability of pigment to reflect the electromagnetic radiation in ultraviolet, visible and near-infrared range. The example of reflectance values of several construction material is shown in figure 2.2. The near-infrared reflectance value is derived from the area under absorption spectrum in near-infrared region in accordance with ASTM standard (Levinson *et al*., 2010).

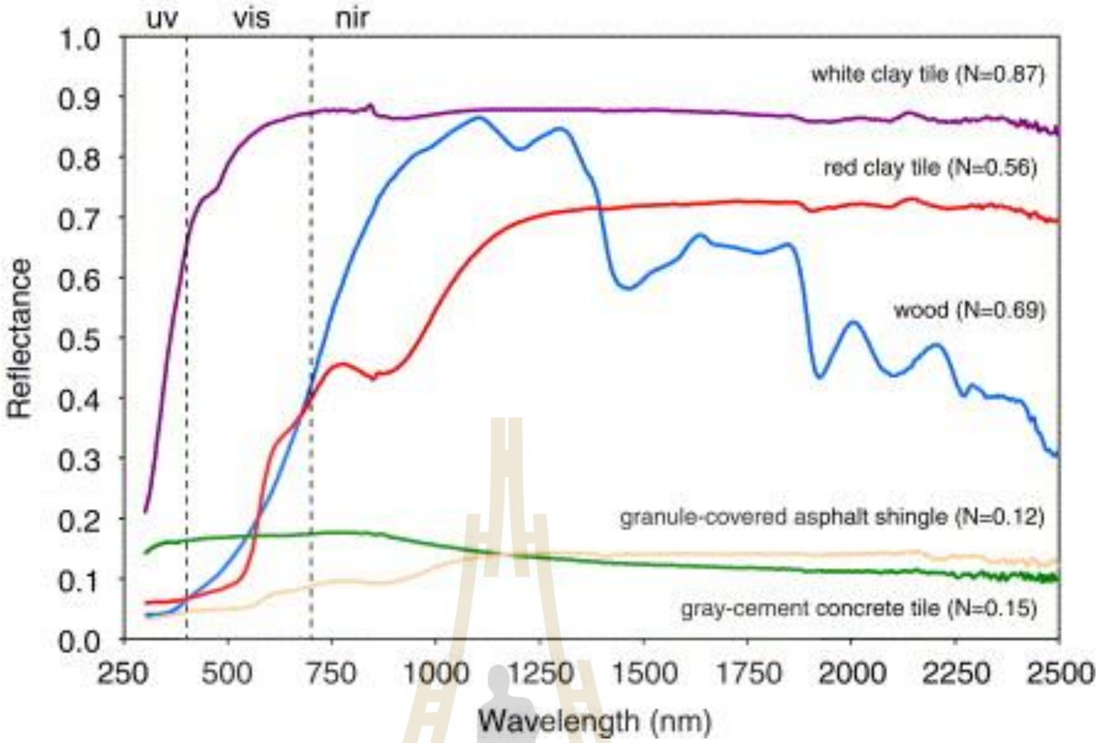

Figure 2.2 Ultraviolet, visible, and near-infrared reflectance of nonmetal constructing materials. The near-infrared (NIR) reflectance values (N) of each material are also shown. (Levinson *et al*., 2007).

The general approach for development of NIR reflective pigment is choosing the parent pigment structure and dope or substitute the element in parent structure by other element to improve NIR reflectance. In most case, the doping or substitution also alter the color of the resulting pigment, for instance, substitution of cerium in $Y_2Ce_2O_7$ pigment by molybdenum can change the color of the pigment from ivory white to yellow at x = 0.5 while the NIR reflectance of the pigment is maintained through this series (Vishnu and Reddy, 2011). In another case, substitution of cerium in $Y_2Ce_2O_7$ pigment by praseodymium changes the color of the pigment to dark brown, however, the NIR reflectance is significantly decreased as the substitution level increase as shown in figure 2.3.

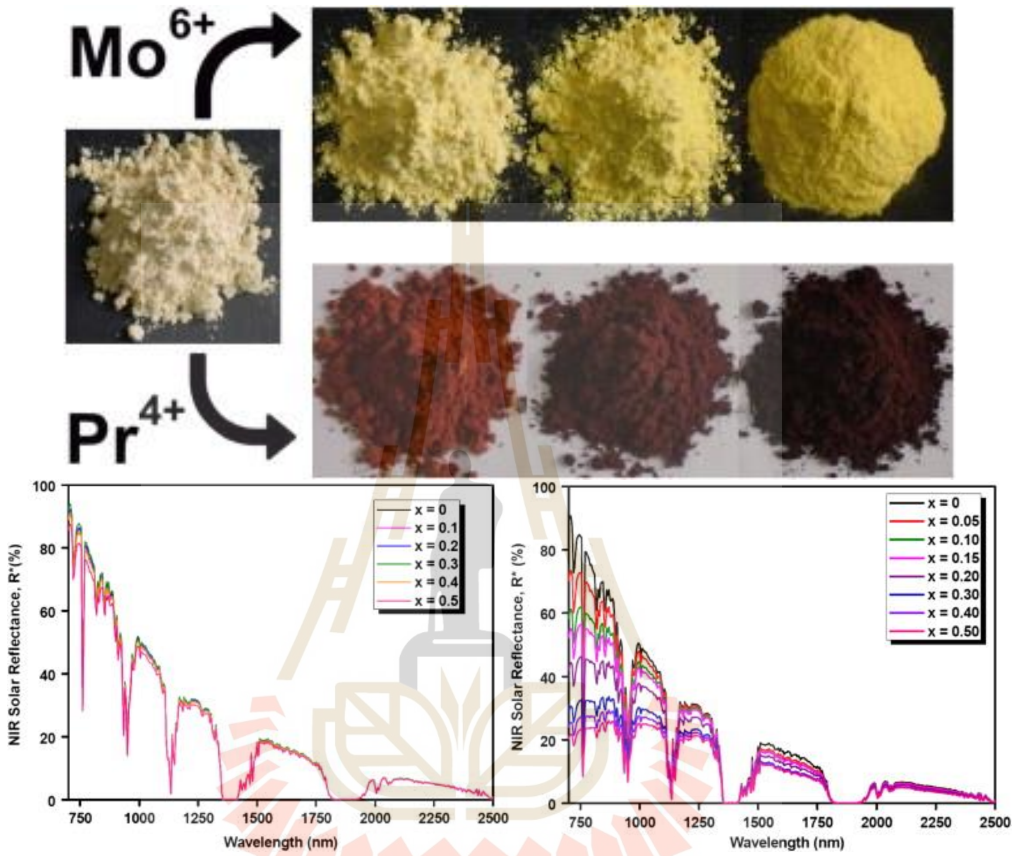

Figure 2.3 Top: Photographs of $Y_2Ce_{2-x}Mo_xO_{7+\delta}$ (x = 0, 0.1, 0.3, 0.5) and $Y_2Ce_{2-x}Pr_xO_7$ (x = 0, 0.1, 0.3, 0.5) pigments. Bottom left: NIR solar reflectance spectra of $Y_2Ce_{2-x}Mo_xO_{7+\delta}$ (x ranges from 0 to 0.5) powder pigments. Bottom right: NIR solar reflectance spectra of $Y_2Ce_{2-x}Pr_xO_7$ powder pigments (Vishnu and Reddy, 2011).

While the substitution of vanadium in $BiVO_4$ parent pigment by tantalum or phosphorus do not significantly change the color tone of the pigment, the NIR reflectance of the yellow pigment is enhanced in both cases (Kumari *et al*., 2013) as shown in figure 2.4.

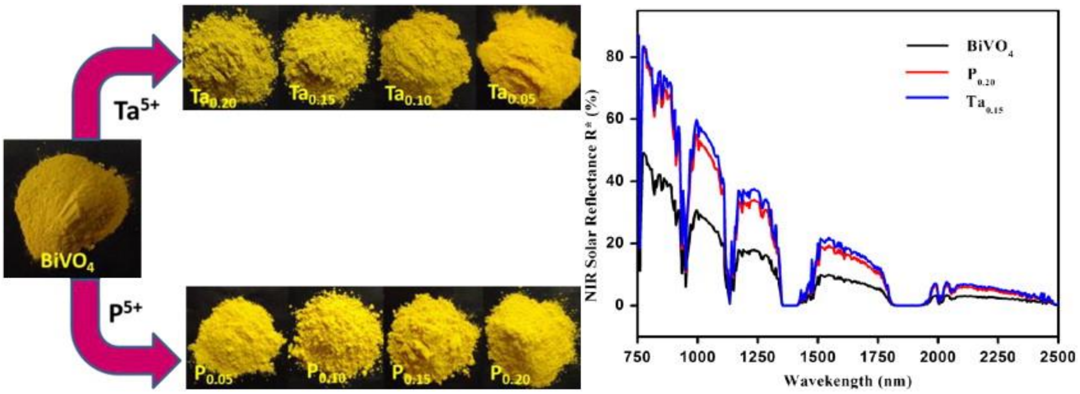

Figure 2.4 Left: Photograph of $BiVO_4$ and $BiV_{1-x}M_xO_4$ (M = Ta and P). Right: NIR solar reflectance spectra of $BiVO_4$, $BiV_{0.85}Ta_{0.15}O_4$, and $BiV_{0.8}P_{0.2}O_4$ yellow pigments (Kumari *et al*., 2013).

Another example is shown in figure 2.5 which show similar strategy to improve NIR reflectance and control the color of the pigment coated on concrete cement. In this case, both $BiFeO_3$ and $BiFe_{0.7}La_{0.3}O_3$ can boost the NIR reflectance compared to traditional coating materials (Yuan *et al*., 2018). From all previous examples, the NIR reflective properties and color of pigment can be altered simultaneously, and the change depends on elemental choice and substitution level.

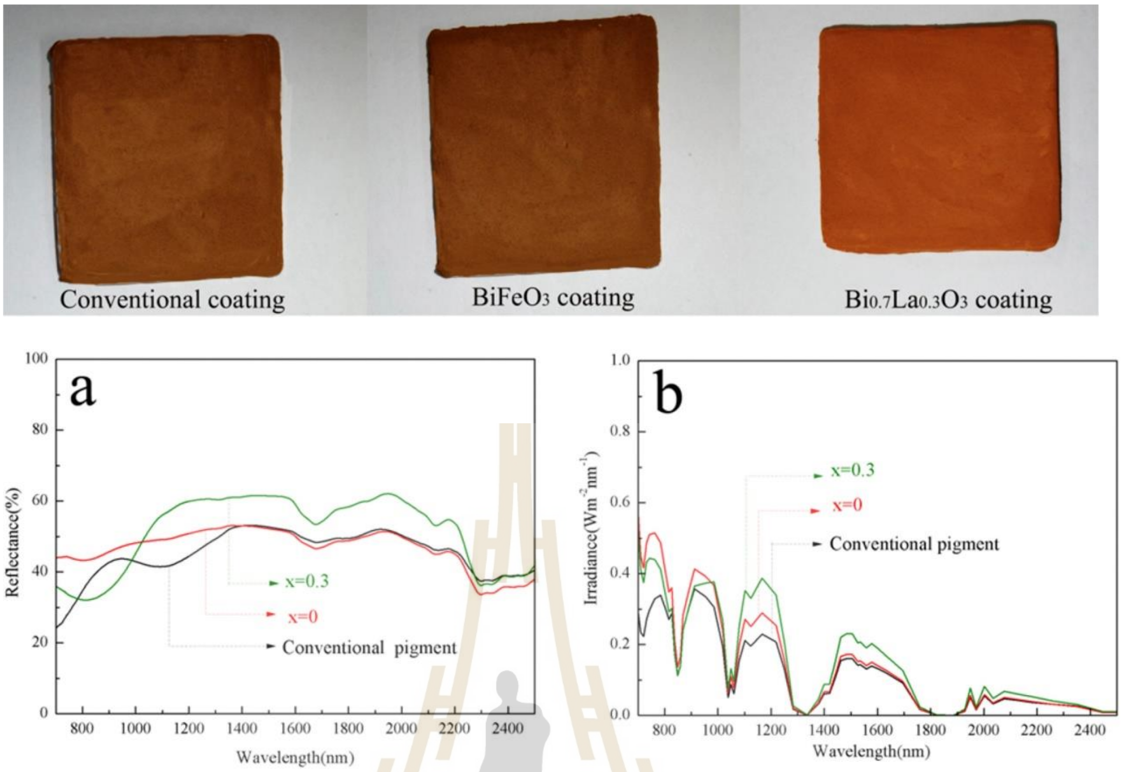

Figure 2.5 Top: Photographs of pigments coated on the concrete cement substrate. Bottom: (a) NIR reflectance and (b) solar radiation energy distribution of the pigmented coatings (Yuan *et al*., 2018).

2.2 Electronic absorption

The energy band of solid crystal is obtained by taking the electron in periodic potential into account. The band structure provides information on several properties of materials, *e.g.*, optical and electrical properties. In electrical sense, the substance can be divided into three main class, shown schematically in figure 2.6, *i.e.*,

1. Conductor, the substance with partially filled band or the valence band and conduction band are overlapped.
2. Insulator, the substance with the absence of the conduction band. In other word, the valence band is fully filled.

3. Semiconductor, the substance with electrical behavior lied between conductor and insulator. Thermal excitation plays a crucial role in conductivity of semiconductor.

The electronic absorption processes of materials in visible and high-frequency infrared regime of electromagnetic spectrum stem from the interband excitation which can be divided into several type, *e.g.*,

1. Intrinsic absorption, the transition occurs from valence band to conduction band, and *vice versa*, in pure semiconductor.
2. Extrinsic absorption, the transition between formal band and donor or acceptor state found in energy band gap.
3. Absorption by defects or impurities state to higher energy state.

All three examples above are the absorption by electronic bound states. However, there is another type of absorption by cloud of free electron called, free carrier absorption which could be considered separately. This is most important in metals and involves the excitation of an electron between two states in the same (partially filled) band.

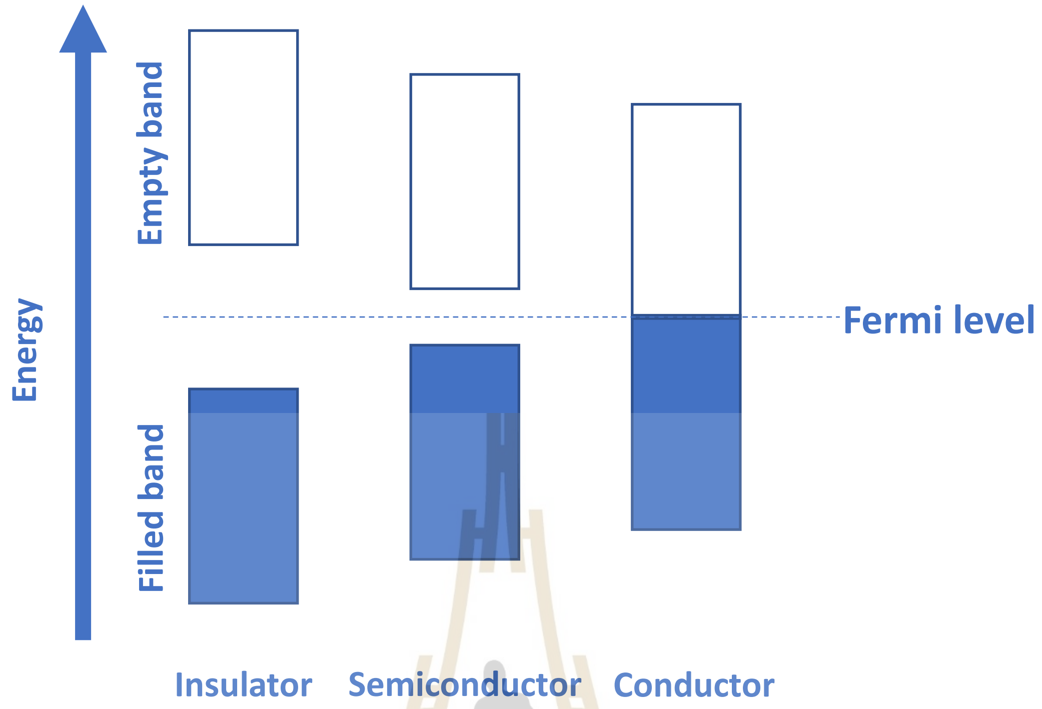

Figure 2.6 Schematic energy diagram representing band structure of material with different electrical properties, *i.e.*, conductor, semiconductor, and insulator.

2.3 Lattice absorption

Lattice absorption is another route for the radiation absorption by materials. The lattice absorption is caused by nonradiative intraband transition of electrons. Lattice absorbs particular frequencies in incident radiation that is resonance with specific natural frequency of each lattice system. The coupling mechanism between the incident photon radiation and the lattice phonon is created by a variation in the electric dipole moment state of the crystal. Hence, energy absorbed from the radiation will be converted into vibrational motion of the atoms.

From electronic absorption and lattice absorption aspects, mentioned in section 2.2 and 2.3, the fundamental assumption in this work is that there are two major contributions to near-infrared reflectance of oxide pigments, i.e., electronic and phononic contributions. From electronic viewpoint, perfect insulator (large energy gap) tends to not absorb almost whole portion of solar radiation. Shifting of Fermi level toward valence band or conduction band, i.e., hole or electron doping, increases material's electrical conductivity which tends to increase the absorption of solar radiation of the material. From phononic consideration, the higher the number and intensity of lattice vibration modes, the more the near-infrared absorption is. By changing the element in the based structure, the frequencies of lattice vibration in the system are altered. The mixing of different frequencies by substitution of other element into system tends to build up the diffuse vibration which in turn decreasing the absorption of near-infrared radiation by lattice vibration. The assumption mentioned above will be used to apply for the explanation of near-infrared behavior in the substitution-level domain.

2.4 Photoemission spectroscopy

Photoemission spectroscopy is a photon-in electron-out type of experiment that is based on photoelectric effect. The technique is popular in surface science characterization due to its specific to surface information and its ability to determine the qualitative and quantitative investigation of elemental properties and oxidation state.

From the basics, photoelectric phenomenon was firstly observed by Hertz in 1887 (Hertz, 1887) and subsequently be explained theoretically by Einstein in 1905 (Einstein, 1905) which is an important part of the foundation of quantum mechanics.

Photoemission spectroscopy was developed under the principle of photelectric effect in 1957 by team of Kai Siegbahn (Nordling, 1957).

The technique is based on photoelectric effect in which the photons with energy greater than the work function of material are capable of ejecting electron by energy transfer process. The escaping electrons will be detected by hemispherical analyzer, where they are counted in a specific energy interval. The equation described the relationship between kinetic energy of ejected electron, E_k, and electron binding energy, E_B, is:

$$E_k = h\nu - E_B - \Phi \qquad (2.1)$$

where Φ is a work function, the energy required for exiting electron at Fermi level to free electron state.

The process occurred during photoemission spectrum measurement is shown in figure 2.7. By using the definite-wavelength photon source with wavelength $h\nu$, the electron the condition matched to the equation 2.1 will be ejected from sample pass through analyzer and finally reach the detector. The electrons at different kinetic energy, differentiated by electron analyzer, will be collected, and recorded as the photoemission spectrum.

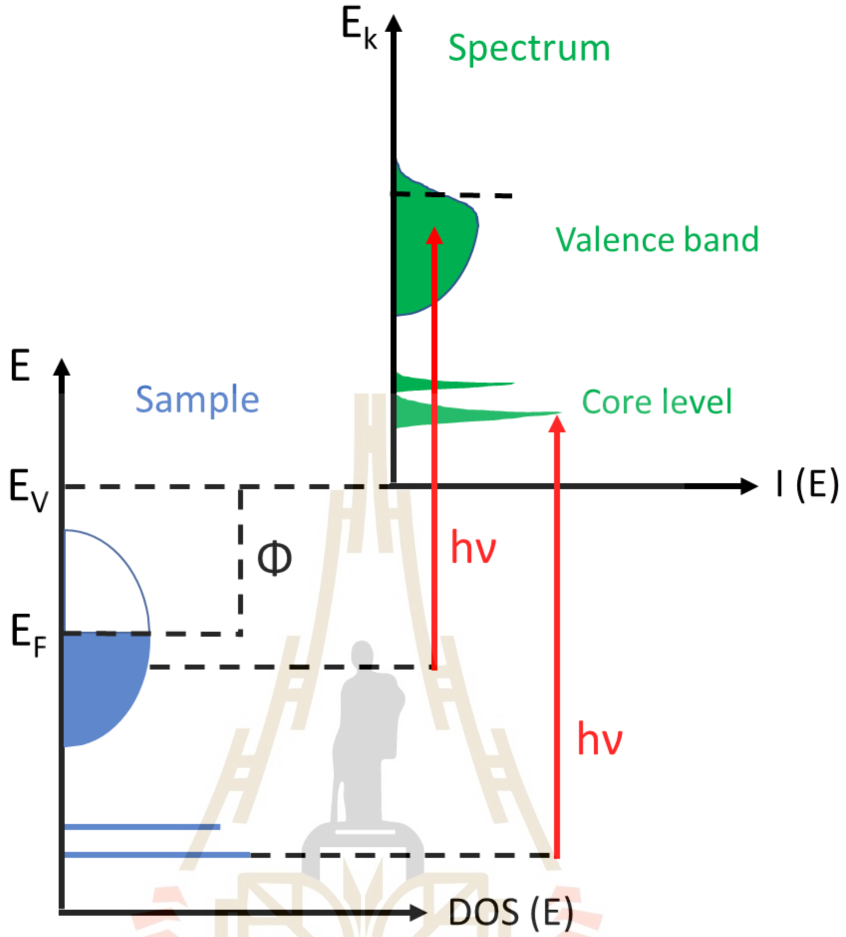

Figure 2.7 Energy diagram showing the photoelectric process during photoemission spectroscopy measurement.

Photoemission spectroscopy is a tool used for the investigation of electronic properties of materials (Roberts and Moffitt, 2019). The technique can provide qualitative information on chemical or oxidation states of interesting elemental component in the sample. It is also used for quantitative analysis of the chemical species in the system. Furthermore, the work function of materials could also be identified by this technique.

2.5 Raman spectroscopy

When light scattered with matter, most fraction of scattered light have the frequency as the incident light, through the elastic scattering process called Rayleigh scattering. Only a small fraction of scattered light show change in frequency compared with incident frequency through the inelastic scattering process called Raman scattering. The frequency modulation from Raman scattering process is related to the vibration mode in molecule or lattice vibration in crystal, the energy loss during inelastic scattering process corresponds to the energy required for the excitation of the system to higher vibrational mode, hence, the information on phonon and vibration can be extracted from Raman scattering measurement.

The difference between scattered frequency and incident frequency, usually lied in far-infrared regime, is called Raman shift. The classification of scattering using the characteristic Raman shift can be divided in to three types, as shown in figure 2.8, *i.e.*,

1. Rayleigh scattering, an elastic scattering with no change in frequency.
2. Stokes scattering, an inelastic scattering with positive Raman shift.
3. Anti-stokes scattering, an inelastic scattering with negative Raman shift.

From the fact that probability of Raman scattering is very low, a high intensity coherent light source, *e.g.*, laser, is required for the excitation in Raman spectroscopy measurement. Raman spectroscopy was used for the characterization of oxide pigments and several other materials (Harroun *et al.*, 2011).

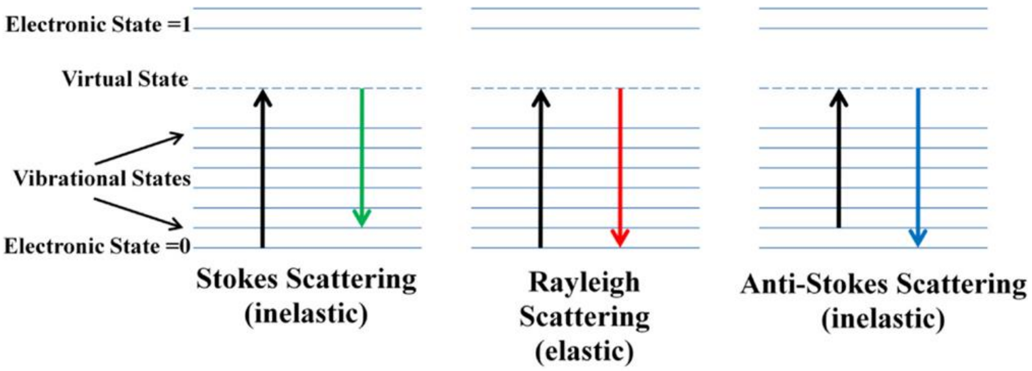

Figure 2.8 Classification of different scattering processes occurred when light interact with matter in far-infrared regime (Lupoi *et al*., 2015).

In detail, the position of Raman scattering peak corresponds to the vibrational frequency of bonding in molecule or lattice in crystal which can be used as a fingerprint investigation of each molecule or crystal. Furthermore, the height of Raman scattering peak corresponds to the strength of molecule/lattice vibration which can imply number of substance concentration or vibration strength of substance.

2.6 Inorganic pigment

Inorganic pigments have been used for aesthetic since the prehistoric time (Orna, 2015). Practically, the paint based on inorganic pigment is the dispersion of insoluble particle in solvent medium (Hund, 1981).

In this work, the pigments used for the electronic and phononic absorption investigation is based on well-known class of inorganic pigment, *i.e.*, oxide compound of iron, aluminum, chromium, and titanium. These pigments are earth abundant compounds and widely used for decoration paints, fabric coloring agent and cosmetics through different era (Orna, 2015). Natural iron oxide was used in caved drawing in ancient time and natural chromium oxide is popular green pigment for painting in renaissance period (Bittler, 1980). Titanium oxide is a newly introduced synthetic white pigment used in paints, coatings, plastics, papers, inks, and toothpastes (van Driel, 2016).

In terms of electrical properties, all pigments used in this work are considered to be either semiconductor or insulator as confirm by the electronic structure study. The band gap of the parent structure species shown in table 2.1, *i.e.*, Cr_2O_3, Al_2O_3, Fe_3O_4, and TiO_2 is 3.2 eV, 7.0 eV, 0.1 eV, and 3.05 eV (Taffa, 2017), respectively.

Table 2.1 The pigment series used for the study of electronic and phononic absorption contribution to near-infrared reflectivity and their associated parent structure compound.

Pigment	**Parent compound**
Ti-substituted Chromium Iron Oxide	Cr_2O_3
$Mg_{1-x}Co_xAl_2O_4$	Al_2O_3
$Zn_{1-x}Co_xFe_2O_4$	Fe_2O_3, Fe_3O_4
$Cr_xSb_xTi_{1-2x}O_2$	TiO_2

Cr_2O_3 with a high NIR-reflectance has been gradually applied to cool building and roofing pigments due to the visual pollution caused by the mainly used white paint and glass for building in urban area. It is required to exhibit green color in the visible spectrum and exhibit the high reflectivity in the near infrared portions of the spectrum to simulate the optical properties of chlorophyll which is considered to be visually comfort compound. Therefore, much interest has attended in preparing Cr_2O_3 with a high NIR reflectance and green color performance (Liang *et al*., 2015). For military application, the green paint used for the camouflage is progressively gaining attention. The development is focused to the simulation of the forest color and adjustment of the near-infrared reflectance of pigment to the level that is comparable to that of environment to avoid the detection by opponent's infrared camera.

Figure 2.9 Photograph of green Cr_2O_3 pigments. (Liang *et al*., 2015).

Iron oxide naturally found in three main crystal phases, *i.e.*, hematite (α-Fe_2O_3), maghemite (γ- Fe_2O_3), and magnetite (Fe_3O_4). The red and yellow hue appearance of the oxide compound of Fe(III) species are resulting from the light absorption in blue and green regime corresponding to electronic band gap of approximately 2.0-2.2 eV in iron oxide compounds. The contribution from scattering and absorption controlled the color of different oxide. Hematite generally appears in bright red while magnetite is naturally black (Cornell and Schwertmann, 2003).

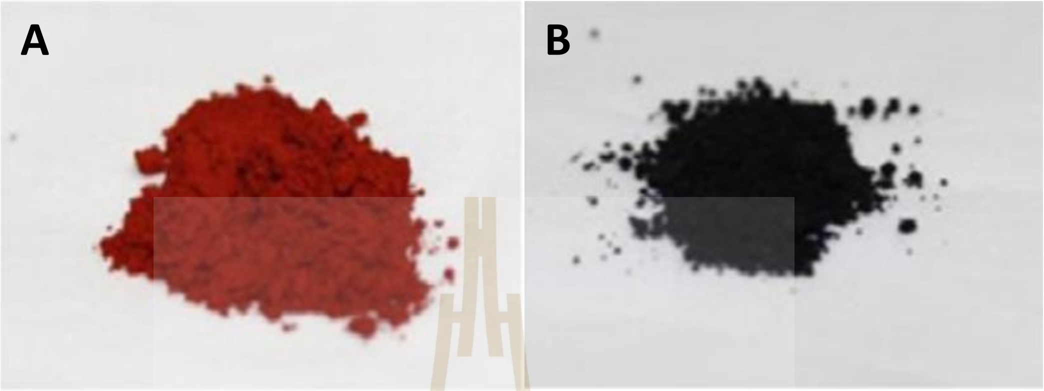

Figure 2.10 Photographs of (A) red Fe_2O_3 (α- Fe_2O_3) and (B) black Fe_2O_3 (γ- Fe_2O_3) pigment. (Voss *et al*., 2020).

Figure 2.11 Photographs of white TiO_2 pigment (Qing *et al*., 2020).

TiO_2 is one of the most used ceramic pigments with high reflection and low absorption of solar radiation. It has broad application prospects in many technologies such as energy conservation building. The doping at relatively high concentration can used for the TiO_2-based pigment color adjustment by introducing defect states as summarized in table 2.2. The type and content of doping element is crucial for the alteration of color hue. Recently, the Co-doping method is utilized for the modifications of TiO_2 color tone by using multiple impurities which could span to more color tone than single doping method (Qing *et al.*, 2020).

Table 2.2 The color of pigment by modification of white TiO_2 pigment using the single doping method with different doping elements (Qing *et al.*, 2020).

Dopant	**Color hue**
Chromium (Cr)	Orange
Manganese (Mn)	Dark brown
Nickel (Ni)	Yellow
Iron (Fe)	Red
Cobalt (Co)	Green
Zinc (Zn)	Green
Vanadium (V)	Gray

Preparation of TiO_2 pigments co-doped with chromium and antimony were report by Zou *et al.* in 2014. The color of the sample underwent a color change from bright yellow to orange as shown in figure 2.12, but the high concentration of doped impurities also caused the NIR reflectivity to drop by about 13%. Overcoming the conflict between VIS and NIR wavebands in doped TiO_2 materials is key to developing colored highly NIR-reflective pigments (Zou *et al*., 2014).

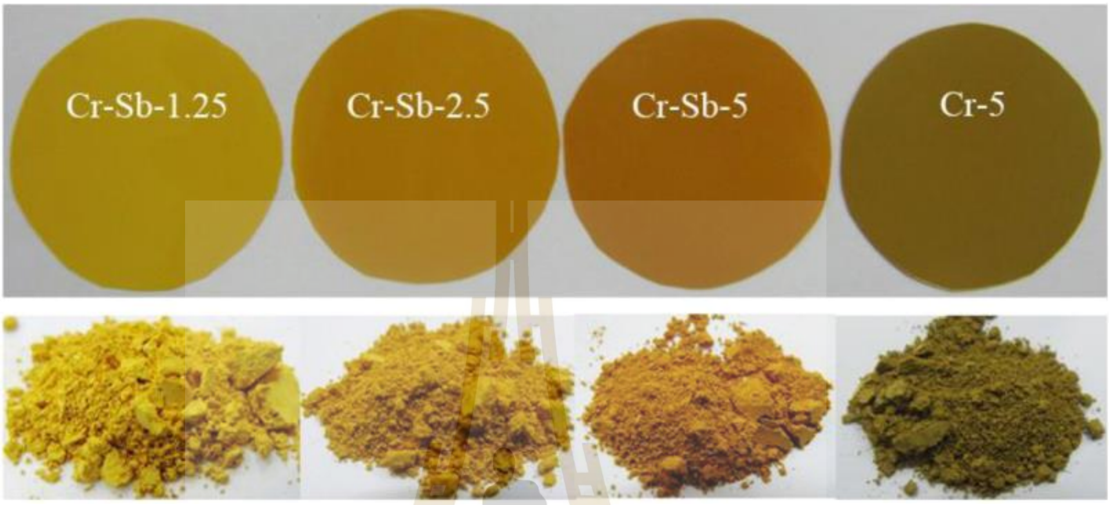

Figure 2.12 Photographs of TiO_2 co-doped with chromium and antimony at different level of doping (Zou *et al*., 2014).

CHAPTER III

RESEARCH METHODOLOGY

The main objective of this research is to distinguish the contributions of electrons and phonons to near-infrared reflectance in oxide ceramic pigments and to evaluate each. We started by preparing four oxide pigment series and confirming their crystal structures. After that, the near-infrared reflectance of pigment samples was examined. The results were compared to independent estimates of electromagnetic absorption by electrons, as indicated by photoemission spectroscopy, and phonons, as indicated by Raman spectroscopy. The details of the experimental protocols in each of these steps are described in this chapter.

3.1 Oxide pigments preparation

The samples used in this work are four series of oxide pigments, *i.e.*, titanium-substituted chromium iron oxide black pigments, $Co_{1-x}Mg_xAl_2O_4$ blue pigments, $Zn_{1-x}Co_xFe_2O_4$ brown pigments and $Cr_xSb_xTi_{1-2x}O_2$ orange pigments, prepared by the solid state reaction method. The detail of each pigment series preparation will be explained in section 3.1.1 – 3.1.4.

3.1.1 Ti-substituted chromium iron oxide

Titanium-substituted chromium iron oxide pigment samples were prepared by mixing the Fe_2O_3, Cr_2O_3 and TiO_2 with the ratio shown in table 3.1. The mixtures were then grinded with wet ball milling to obtain fine homogeneous powder. The powder was dried at 100 °C for 60 minutes before calcined at 1250 °C for 3 hours. The obtained oxide samples were then cooled down and subsequently washed with deionized water followed by drying and sieving with 325-mesh sieve.

Table 3.1 Composition of raw material used for preparation of titanium-substituted chromium iron oxide black pigments.

Sample (%Ti)	Fe_2O_3 (wt.%)	Cr_2O_3 (wt.%)	TiO_2 (wt.%)
0%	40.0	60.0	0
2%	40.0	58.0	2.0
4%	40.0	56.0	4.0
6%	40.0	54.0	6.0
8%	40.0	52.0	8.0

3.1.2 $Co_{1-x}Mg_xAl_2O_4$

$Co_{1-x}Mg_xAl_2O_4$ pigment samples were prepared by mixing the Co_2O_3, MgO and Al_2O_3 with the ratio shown in table 3.2. The mixtures were then grinded with wet ball milling to obtain fine homogeneous powder. The powder was dried at 90°C for 60 minutes before calcined at 1200 °C for 3 hours. The obtained oxide samples were then cooled down and subsequently washed with deionized water followed by drying and sieving with 325-mesh sieve.

Table 3.2 Composition of raw material used for preparation of $Co_{1-x}Mg_xAl_2O_4$ pigments.

Sample	Co_3O_4 (mol)	MgO (mol)	Al_2O_3 (mol)
x = 0	0	1.000	1.000
x = 0.05	0.017	0.950	1.000
x = 0.1	0.033	0.900	1.000
x = 0.2	0.067	0.800	1.000
x = 0.4	0.133	0.600	1.000
x = 0.6	0.200	0.400	1.000
x = 0.8	0.267	0.200	1.000
x = 1.0	0.333	0	1.000

3.1.3 $Zn_{1-x}Co_xFe_2O_4$

The $Zn_{1-x}Co_xFe_2O_4$ pigment samples were prepared by mixing the Fe_2O_3, ZnO and Co_3O_4 with the ratio shown in table 3.3. The mixtures were then grinded with wet ball milling for 5 hours to obtain fine homogeneous powder. The powder was dried at 100 °C for 60 minutes before calcined at 1100 °C for 3 hours with temperature ramping rate at 5 °C/minute. The obtained oxide samples were then cooled down and subsequently washed with deionized water followed by drying and sieving with 325-mesh sieve.

Table 3.3 Composition of raw material used for preparation of $Zn_{1-x}Co_xFe_2O_4$ pigments.

Sample	ZnO (mol)	Co_3O_4 (mol)	Fe_2O_3 (mol)
x = 0	1.000	0	1.000
x = 0.1	0.900	0.033	1.000
x = 0.3	0.700	0.100	1.000
x = 0.5	0.500	0.167	1.000
x = 0.7	0.300	0.233	1.000
x = 0.9	0.100	0.300	1.000

3.1.4 $Cr_xSb_xTi_{1-2x}O_2$

$Cr_xSb_xTi_{1-2x}O_2$ pigment samples were prepared by mixing the Cr_2O_3, Sb_2O_3 and TiO_2 with the ratio shown in table 3.4. The mixtures were then grinded with wet ball milling to obtain fine homogeneous powder. The powder was dried at 90 °C for 60 minutes before calcined at 1200 °C for 3 hours. The obtained oxide samples were then cooled down and subsequently washed with deionized water followed by drying and sieving with 325-mesh sieve.

Table 3.4 Composition of raw material used for preparation $Cr_xSb_xTi_{1-2x}O_2$ pigments.

Sample	Cr_2O_3 (mol)	Sb_2O_3 (mol)	TiO_2 (mol)
x = 0.024	0.012	0.012	0.951
x = 0.048	0.024	0.024	0.905
x = 0.057	0.028	0.028	0.887
x = 0.091	0.045	0.045	0.818
x = 0.167	0.083	0.083	0.667
x = 0.286	0.143	0.143	0.429
x = 0.375	0.188	0.188	0.250

3.2 Crystal structure evaluation by x-ray diffraction

The samples were characterized by x-ray diffraction to investigate the crystal structure and phase. The diffractogram was recorded in the 2Θ range of 20-80 degree with a step size of 0.05 degree.

3.3 Near-infrared reflectance evaluation from UV-Vis-NIR bsorption spectrophotometry

Near-infrared reflectance is evaluated for the quantification of the capability of pigment to reflect the electromagnetic radiation in near-infrared region. Near-infrared reflectance of each sample was derived from near-infrared absorption spectrum in the wavelength ranged from 700 to 2500 nm in accordance with ASTM standard E903.

3.4 Investigation of potential for electronic absorption by x-ray photoemission spectroscopy

The x-ray photoemission spectroscopy is used for the electronic properties of pigment. The measurements were carried out by PHI 5000 VersaProbe II x-ray photoelectron spectrometer using x-ray source with energy 1486.6 eV at beamline 5.3, Synchrotron Light Research Institute (SLRI), Thailand.

3.5 Lattice absorption investigation by Raman spectroscopy

Raman spectroscopy is used for the investigation of lattice absorption in pigment. Raman spectroscopy measurement of oxide pigment samples were observed by Bruker Senterra dispersive Raman microscope. The light source used for the measurement in $Cr_xSb_xTi_{1-2x}O_2$ sample set is 532 nm laser. The light source used for the measurement in titanium-substituted chromium iron oxide, $Zn_{1-x}Co_xFe_2O_4$ and $Co_{1-x}Mg_xAl_2O_4$ sample set is 785 nm laser. The excitation wavelength was chosen based on the maximization of Raman signal intensity.

3.6 Miscellaneous characterizations

Fourier-transform infrared spectroscopy (FTIR) was employed for preliminary evaluation of lattice vibration contribution in ceramics pigments. The data were recorded by Bruker FT-IR spectrometer in wave number range of 4000-400 cm^{-1} using attenuated total reflection (ATR) mode. Electrical capacitance and loss tangent were recorded using Impedance analyzer (Agilent 4294A) for the preliminary study of electronic contribution in ceramics pigments.

3.7 Data analysis

Near-infrared reflectance percentage was calculated from near-infrared spectra, in range of 700-2500 nm, obtained from UV-Vis-NIR spectrophotometry measurement. The calculation is based on the ASTM standard E903 with the formula for near-infrared reflectance, *R* is:

$$R = \frac{\int_{700}^{2500} r(\lambda)\mathrm{i}(\lambda)\,d\lambda}{\int_{700}^{2500} \mathrm{i}(\lambda)\,d\lambda} \qquad (3.1)$$

where r(λ) is the experimentally obtained spectral reflectance (Wm^{-2}) and i(λ) is the solar spectral irradiance ($\mathrm{Wm}^{-2}\mathrm{nm}^{-1}$).

The integrated Raman signal area was calculated from Raman spectrum by integration of Raman scattering intensity over specific Raman shift range using sum function in Igor Pro 6.3 (WaveMetrics) software.

The valence band maximum positions were tracked manually from calibrated valence band signal with background signal subtraction by using the position at half height of the nearest band to Fermi level.

The correlation coefficients between electronic/phononic properties and near-infrared reflectance were calculated by using Pearson product-moment correlation coefficient, ρ. For a pair of electronic/phononic related properties (P) and near-infrared reflectance (R) variables, the formula for ρ is:

$$\rho_{P,R} = \frac{Cov(P,R)}{\sigma_P \sigma_R} \qquad (3.2)$$

where $Cov(P,R)$ is covariance of electronic/phononic related properties (P) and near-infrared reflectance (R). σ_P and σ_R are standard deviation of electronic/phononic related properties and near-infrared reflectance, respectively.

CHAPTER IV

RESULTS AND DISCUSSION

The results and discussion on preparation, crystal structure confirmation, near-infrared reflectance and electronic/phononic(lattice) behavior are grouped by pigment set through section 4.1-4.4. The core idea of this work, the correlation between electronic/phononic behavior and near-infrared reflectance, are then discussed and summarized in the last section, section 4.5.

4.1 Titanium-substituted chromium iron oxide pigments

The first pigment series that were studied in this work are black chromium iron oxide pigments with partially substituted by titanium from 0% to 8% and calcined at 1250 °C. The color appearance of as-prepared titanium-substituted chromium iron oxide pigments is show in figure 4.1. The color of pigments in this series is not changed much along substitution by titamium from 0% to 8% which would primarily be implied that there is very little or no change in electronic gap for up to 8% titanium substitution in this system.

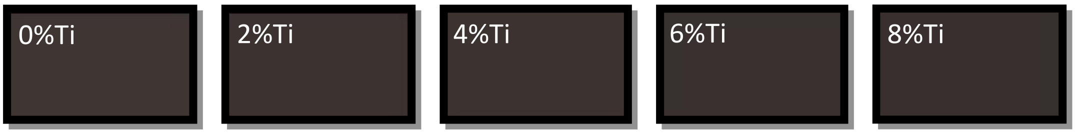

Figure 4.1 Color of titanium-substituted chromium iron oxide pigments with titanium substitution level from 0% to 8%.

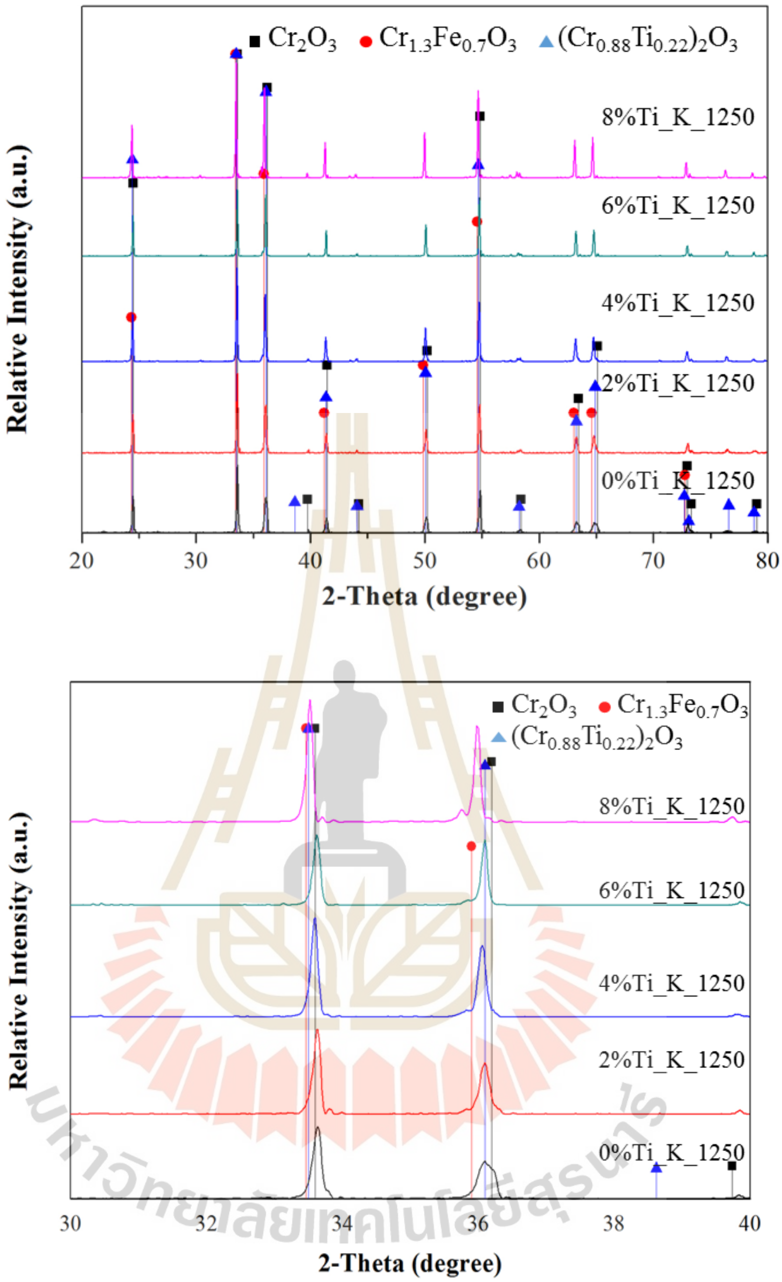

Figure 4.2 X-ray diffractogram of titanium-substituted chromium iron oxide pigments with titanium substitution level from 0% to 8%.

The crystal structure of titanium-substituted chromium iron oxide pigment samples, characterized by x-ray diffraction, was deduced from diffractograms shown in figure 4.2. By using XRD pattern matching approach, there are 3 potential structures that play a role in this system, *i.e.*, $Cr_{1.3}Fe_{0.7}O_3$ (ICDD# 00-035-1112), $(Cr_{0.88}Ti_{0.12})_2O_3$ (ICDD# 01-082-0211), and Cr_2O_3.

According to the assumption proposed in this study, the fundamental properties that govern near-infrared reflectance is electronic and phononic(lattice) behavior. In order to acquire electronic properties of the pigments, we firstly employed electrical impedance measurement for the preliminary study. The electrical properties obtained from impedance analyzer in this study are electrical capacitance and loss tangent. Due to the requirement for electrical capacitance measurement, the sample has to be in a rigid form with very smooth surface and we must be able to find the accurate sample thickness and contacting surface area between sample and electrode. All as-prepared pigments from solid state reaction are in powder form, hence, we have to press the fine powder of sample to the rigid pellet form by using hydraulic press.

The samples after pressed at pressure 5 MPa with 5 minutes pressing time were shown in figure 4.3. The radial crack was observed in several sample pellets which cannot be used for measurement. However, the sample with very low degree of cracking cannot be transferred to measurement system due to the brittle and fragile surface which also cannot be used for the reliable electrical capacitance measurement. Hence, we have to optimize the pressing condition and post-pressing treatment of these black pigment samples. By annealing with 600 °C and 5 hours under argon atmosphere in tube furnace, the samples show lower degree of cracking with bent surface (shown in figure 4.4), however, they are vulnerable to be safely transferred to measurement unit. The crack along circumference line slowly extended to sample center over time.

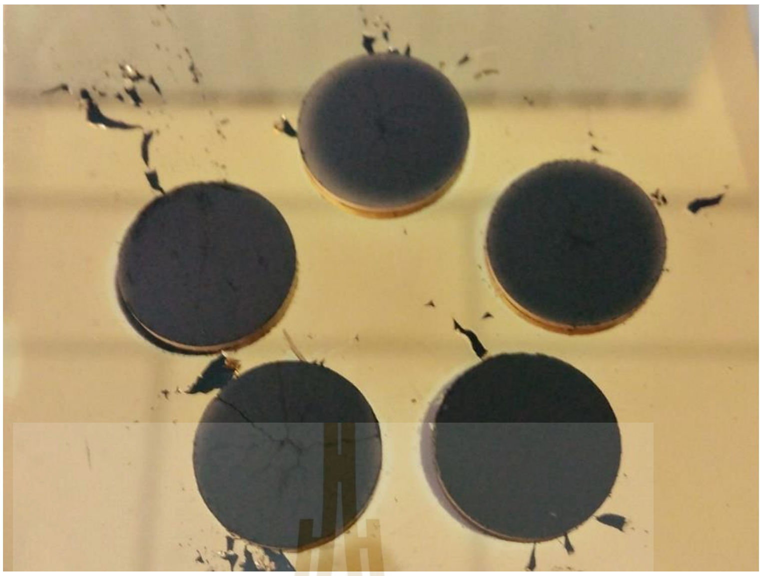

Figure 4.3 Five titanium-substituted chromium iron oxide pigment pellets after hydraulic pressed at 5 MPa for 5 minutes (After gold coating by DC sputtering).

Figure 4.4 Five titanium-substituted chromium iron oxide pigment pellets after hydraulic pressed at 5 MPa for 5 minutes followed by annealing at 600 °C for 5 hours under argon atmosphere.

The results from hydraulic pressing of pigment sample are not satisfied. The obtained pellet does not meet the requirement for reliable electrical measurement by impedance analyzer. We cannot employ this approach for electrical properties investigation; hence, we need to find another method that match our limitation in sample form. We decided to use photoemission spectroscopy to extract the information on electronic properties of pigment series which will be discussed afterward.

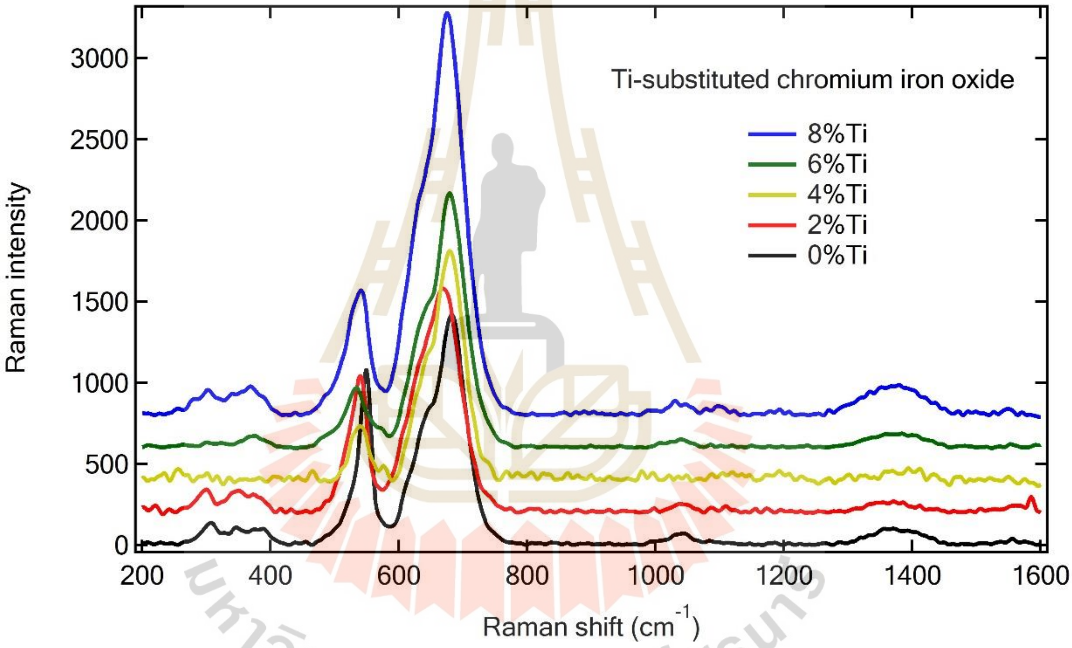

Figure 4.5 Raman spectra of titanium-substituted chromium iron oxide pigment calcined at 1250 °C with titanium concentration in range of 0-8%w/w.

Another contribution from our assumption is phononic contribution. We straightforwardly proposed that the number of vibration mode and vibration intensity observed from Raman signal is directly proportional to absorption by lattice/phonon and inversely proportional to the reflectance. It would be easy if we can find a single number represented the number of vibration mode and vibration intensity observed from Raman signal. Hence, we decide to use the area under Raman spectra obtained from the integration of Raman signal in signal detected range as a representation of number of vibration mode and vibration intensity. Raman spectra shown in figure 4.5 is spectra from titanium-substituted chromium iron oxide pigment which are calcined at 1250 °C for 3 hours with titanium concentration ranged from 0% to 8%w/w. We found Raman scattering signal in Raman shift range of 200-1500 cm^{-1}, corresponds to energy range of 25-185 meV.

The relationship between Area under Raman signal, integrated from 200 to 1600 cm^{-1}, and near-infrared reflective percentage of titanium-substituted chromium iron oxide is shown in figure 4.6. The overall relationship could be preliminary seen as the negative correlation of these two quantities. The negative correlation of lattice between lattice absorption, probed via Raman scattering signal area, and near-infrared reflectance can be explained by that the higher lattice absorption, the lower near infrared reflectance. This interpretation is straightforward in case that transmission of electromagnetic wave through materials is negligible and will be applied for qualitative analysis of change in near-infrared reflectance throughout this work.

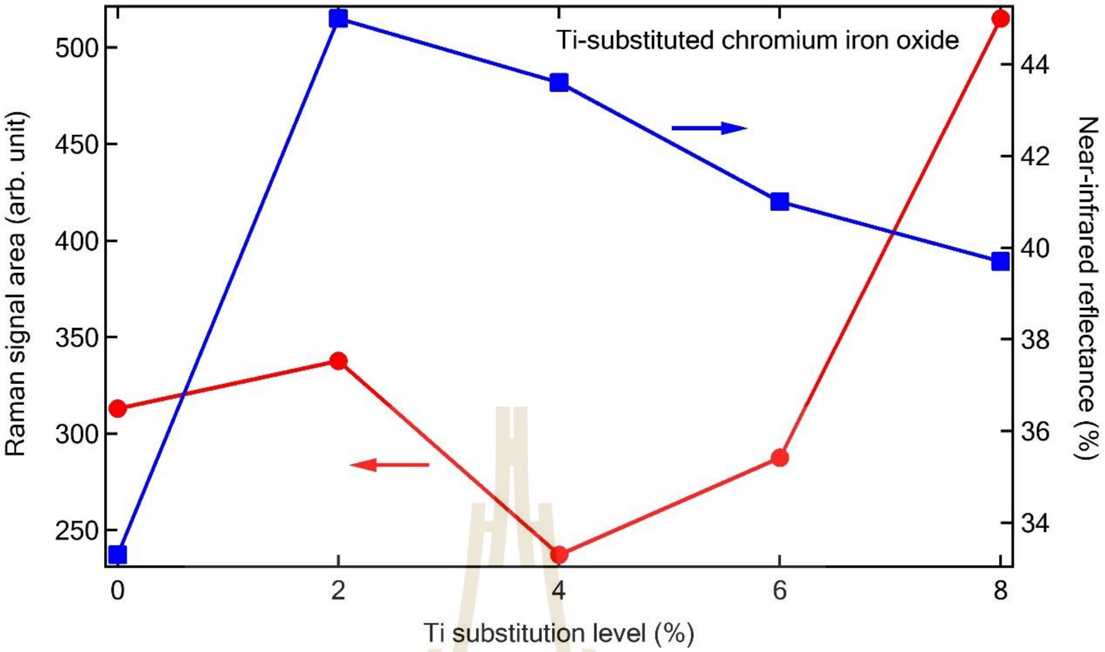

Figure 4.6 Raman scattering signal area integrated over 200-1600 cm^{-1} range (red circle, left axis) and near-infrared reflectance (blue square, right axis) as a function of titanium substitution level in titanium-substituted chromium iron oxide.

From the limitation in pigment pellet processing, as discussed earlier, we cannot employ the direct electrical measurement. The photoemission spectroscopy is our next candidate for the electronic behavior investigation. The photoemission spectroscopy is analytical technique that can provide information on occupied electronic energy state. We have focused on the energy state near Fermi level which the area that can use for the evaluation of electrical and electronic properties. In other word, the valence band maximum, extracted from photoemission spectra, can be used to determine the conductivity which can be further imply the potential for electronic absorption which will be discussed along the results. We strictly use the word “potential” because the photoemission spectroscopy can provide data only in the occupied state, not include the unoccupied state, hence, we cannot extract the information about energy band gap.

Then the maximum position of occupied state relative to Fermi level will be used for the evaluation of conductivity and “potential” of electronic absorption, i.e., the higher the valence band maximum, the higher the conductivity and stronger the potential for electronic absorption by the system which lead to the more intense color appearance of the pigment.

Valence band region, obtained from photoemission spectroscopy, revealed the independent of titanium composition on valence band position as observed from the barely changed photoemission spectra, shown in figure 4.7, of titanium-substituted chromium iron oxide of valence band peak position as well as valence band maximum position upon increasing titanium substitution percentage.

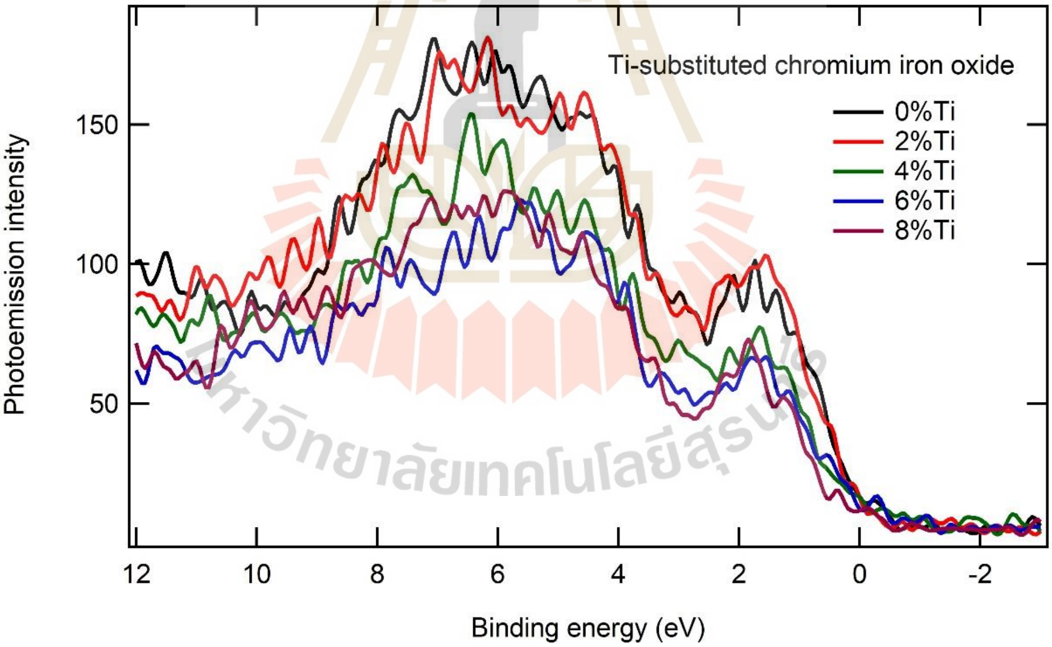

Figure 4.7 Photoemission spectra in valence band (VB) region of titanium-substituted chromium iron oxide pigments with titanium concentration in range of 0-8%w/w.

However, by carefully tracking the energy with half-intensity of first valence band peak, we found that there is a trend of valence band maximum changing as shown in figure 4.8. From 2% to 8% titanium concentration. The trend of these two quantities tend to move in opposite direction which can primarily indicate the contribution of electronic properties to near-infrared reflectance of this system.

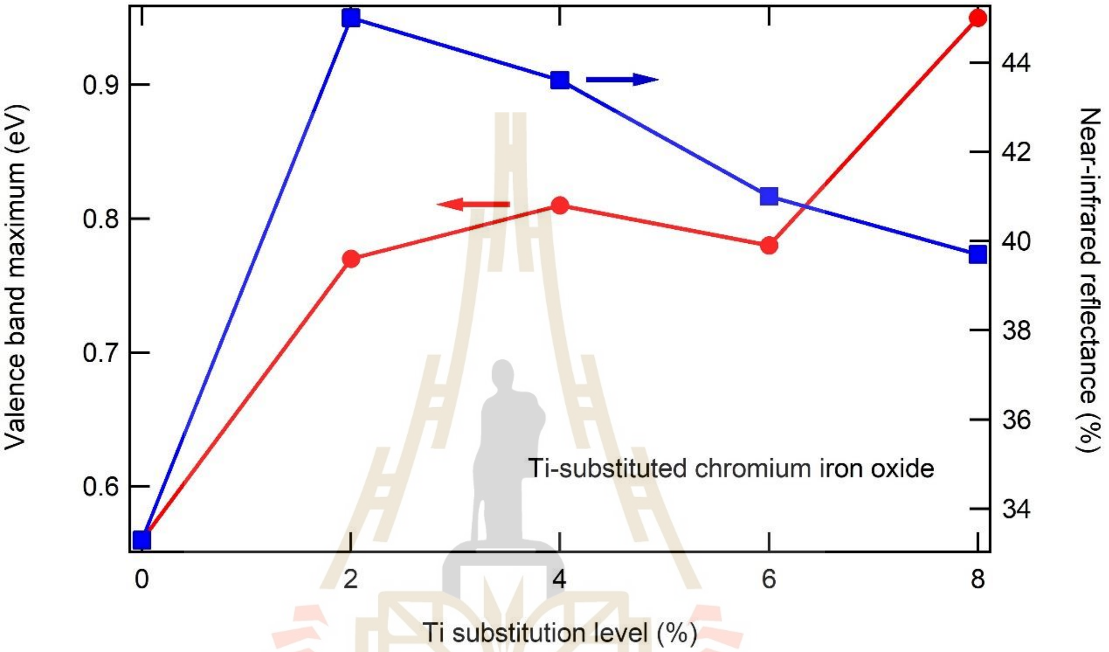

Figure 4.8 Valence band maximum (red circle, left axis) and near-infrared reflectance (blue square, right axis) as a function of titanium substitution level in titanium-substituted chromium iron oxide.

Photoemission spectra of titanium-substituted chromium iron oxide in titanium core level regime, shown in figure 4.9, indicate the increasing of the intensity of titanium as the titanium concentration in the pigments increased. While the position of titanium signal barely change by the titanium concentration which can implied that oxidation state of titanium is barely changed by the level of titanium addition in the range studied by this work.

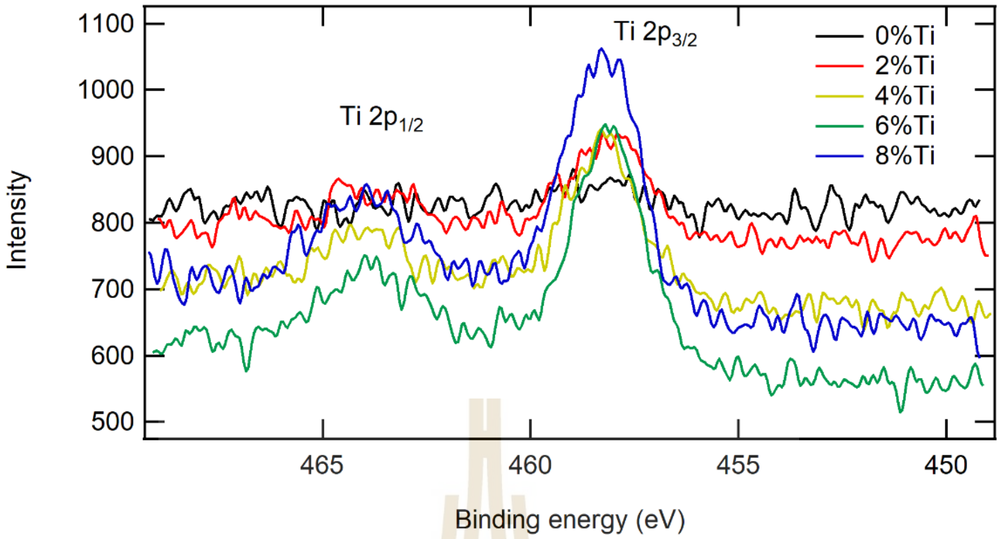

Figure 4.9 X-ray photoelectron spectra in titanium (Ti) core level regime titanium-substituted chromium iron oxide.

Furthermore, we also found similar behavior in iron core level and chromium core level regime, as shown in figure 4.10 and 4.11, respectively. The core level peaks are barely change by the effect of titanium concentration in both cases.

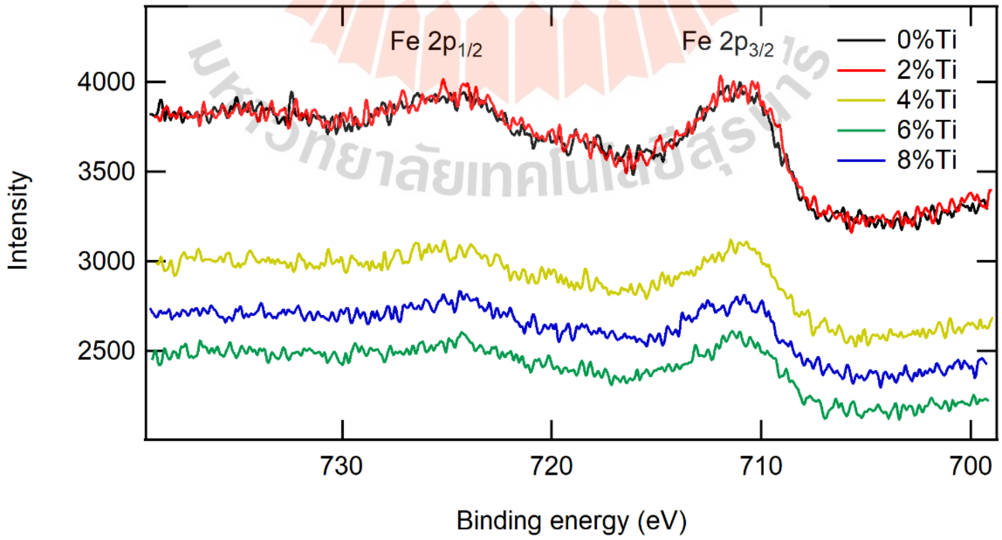

Figure 4.10 X-ray photoelectron spectra in iron (Fe) core level regime titanium-substituted chromium iron oxide.

From all core level spectra, in summary, we found that oxidation state of all three elemental components in titanium-substituted chromium iron oxide system is barely change by the concentration of titanium added to the sytem, up to 8 w%. This summary is reflected by that the color of all pigment member in this series is very similar to each other.

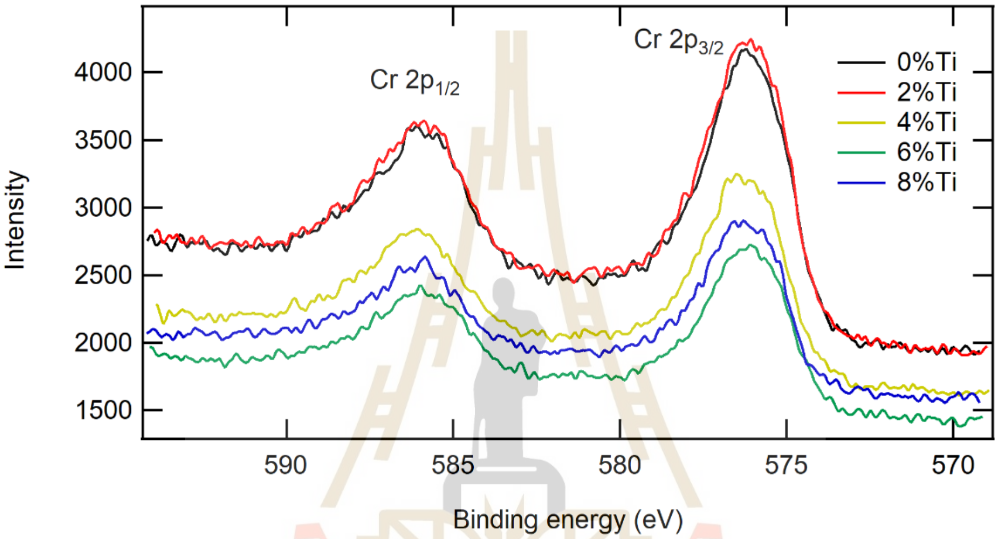

Figure 4.11 X-ray photoelectron spectra in chromium (Cr) core level regime titanium-substituted chromium iron oxide.

From XPS wide scan, the additional signal of silicon and cobalt which is not the base components of this system are observed. Cobalt core level spectra, shown in figure 4.12, indicate the increment of cobalt concentration, confirmed by the increasing of XPS intensity, as titanium percentage increased. Consequently, the presence of cobalt would be due to the cobalt impurities in industrial grade titanium precursor used in titanium-substituted chromium iron oxide preparation. However, it should be stressed that by carefully track the valence band maximum position, as we discussed earlier, there is a trend of change in valence band position along substitution level and this might be true for core level spectra but this is not in the scope of this work.

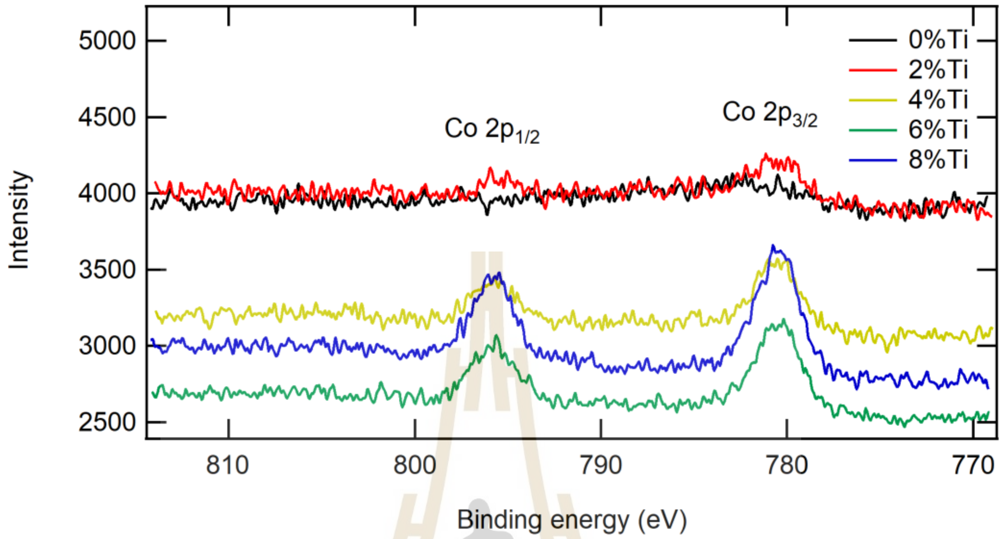

Figure 4.12 X-ray photoelectron spectrum in cobalt (Co) core level regime of titanium-substituted chromium iron oxide pigments.

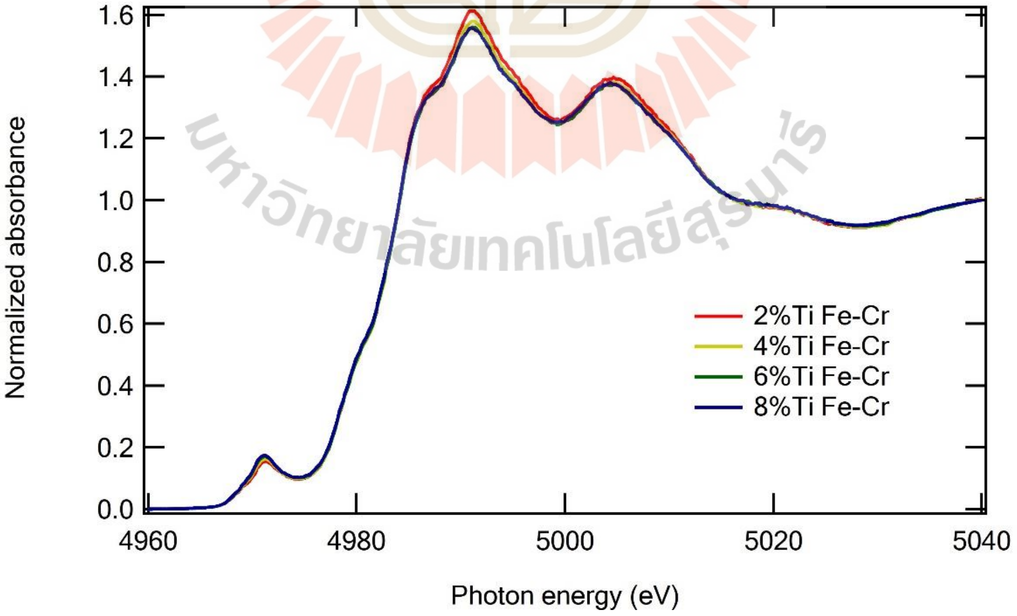

Figure 4.13 Titanium *K*-edge XANES spectra of titanium-substituted chromium iron oxide pigments.

We can extract the information about oxidation state or valence state and local symmetry around interesting element from XANES spectrum. In titanium-substituted chromium iron oxide pigments, titanium atom is the minority component that was introduced to the parent chromium iron oxide structure. At very low level of titanium concentration, titanium's local environment would qualitatively be similar to that of chromium atom. On the other hand, at higher titanium concentration, the probability of local symmetry breaking becomes significantly larger. Hence, probing local environment via minority atom would show significant change that could facilitate the electronic and structural interpretation.

From XANES spectra, shown in figure 4.13, the absorption edges reveal the existence of both Ti^{3+} and Ti^{4+} oxidation state for all titanium-contained sample. All samples exhibit similar XANES features. There is an increasing of pre-edge intensity as the titanium level increasing that could refer to the decreasing of local symmetry around titanium atom as the titanium concentration increased.

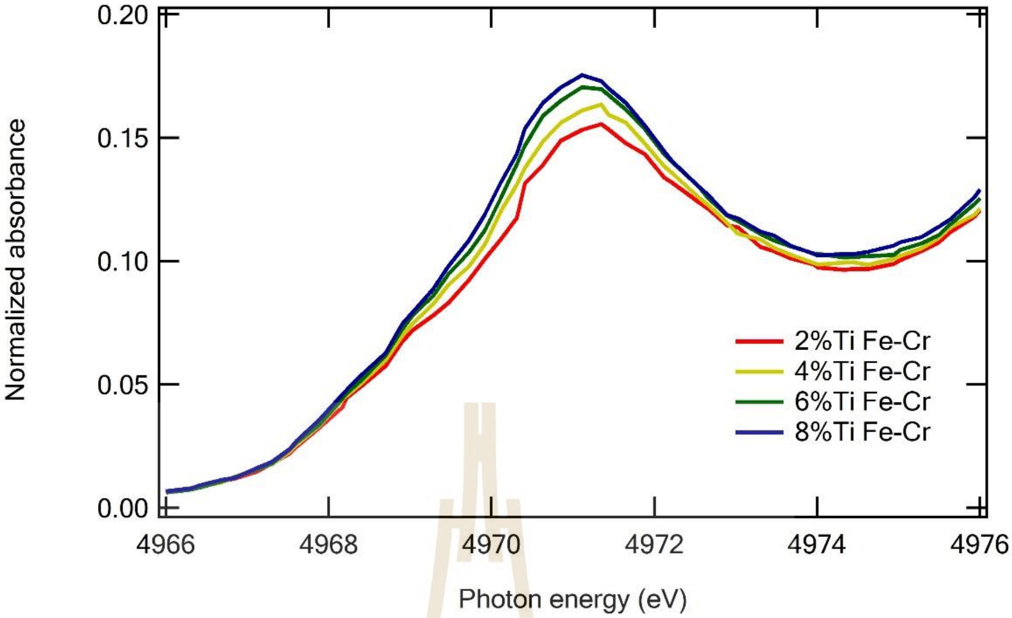

Figure 4.14 Pre-edge region of titanium *K*-edge XANES spectra of titanium-substituted chromium iron oxide pigments.

From pre-edge regime, shown in figure 4.14, the intensity of pre-edge feature increases upon titanium concentration in titanium-substituted chromium iron oxide structure increasing. The pre-edge excitation of *K*-edge region corresponds to the excitation of electron from 1*s* to 3*d* state which is, according to electronic transition selection rule, a forbidden transition, hence, the intensity of pre-edge excitation is relatively low (For ideal case, the intensity of pre-edge peak in transition metal oxide approaches zero) compared to the selection rule-allowed main transition, 1*s* to 4*s* state, at absorption edge. The probability of transition from 1*s* to 3*d* is zero for pure final 3*d* state. The non-zero intensity pre-edge peak in transition metal oxide compounds stems from the hybridization of 3*d* orbital of transition metal with 2*p* orbital of oxygen. Non-zero *p*-character in *d*-*p* hybridized leads to non-zero pre-edge peak intensity.

Another factor that influences the intensity of pre-edge feature is local symmetry around interesting atom. The higher the local symmetry, the lower pre-edge peak intensity. In case of titanium-substituted chromium iron oxide, the increasing of pre-edge intensity refers to the decreasing of local symmetry around titanium site. This change could be explained by the increasing of probability for finding adjacent titanium pair. We found that titanium atoms are introduced into titanium-substituted chromium iron oxide structure in place of chromium atom which is surrounded by 6 atoms in first nearest neighbour shell. The increasing of titanium concentration in the structure leads to the increasing number of titanium atom with broken neighbouring atom symmetry which in turn decreases the local symmetry around titanium atom and eventually increases the pre-edge peak intensity.

4.2 $Co_{1-x}Mg_xAl_2O_4$ pigments

The color and appearance of as-prepared $Co_{1-x}Mg_xAl_2O_4$ pigments were shown in figure 4.15. As the magnesium content increased, the color of the pigment changes from dark navy blue, for x = 0, to blue shade at moderate magnesium concentration. By completely replace the cobalt by magnesium, the pigment turns bright white, x = 1.0. The intensity of pigment color is monotonically brightened by magnesium concentration.

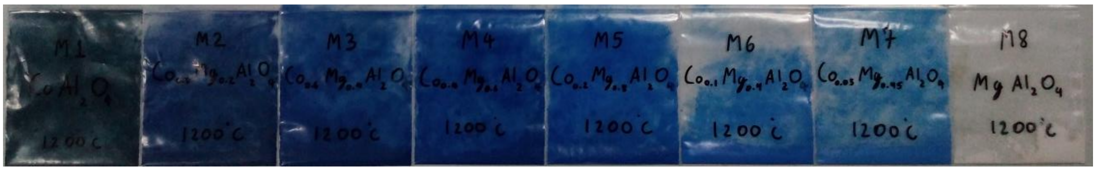

Figure 4.15 Color appearance of $Co_{1-x}Mg_xAl_2O_4$ pigment calcined at 1200 °C.

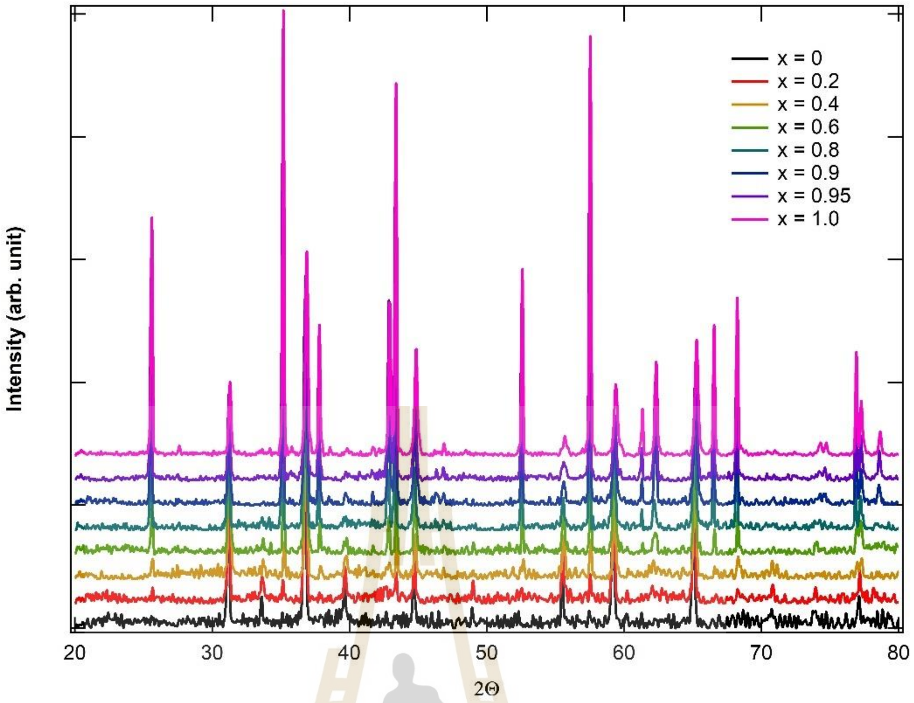

Figure 4.16 XRD patterns of $Co_{1-x}Mg_xAl_2O_4$ pigment calcined at 1200 °C.

Raman spectra shown in figure 4.17 are collected from $Co_{1-x}Mg_xAl_2O_4$ blue pigment samples calcined at 1200 °C with x equals to 0, 0.2, 0.4, 0.6, 0.8, 0.9, 0.95 and 1.0, respectively. Raman scattering signal in wavenumber range of 150-800 cm^{-1} (corresponds to energy approximately 20-100 meV) were found in every sample in this series except for that of the $MgAl_2O_4$ sample which show no signal over 100-4000 cm^{-1} range. By plotting area under Raman spectrum signal and near-infrared reflectance percentage (%R) against the magnesium substitution level as shown in figure 4.18, we found that the Raman signal area is inversely proportional to near-infrared reflectance. The Raman signal area directly indicates far infrared absorptivity of the pigment which is inversely proportional to the reflectance (in case that the transmission plays no role). Moreover, the energy of these Raman peak corresponds to the energy related to phonon excitation energy which also related to the lattice vibration. In summary, this negative correlation indicates the strong negative correlation between the phonon absorption and near-infrared reflectance of $Co_{1-x}Mg_xAl_2O_4$ pigments.

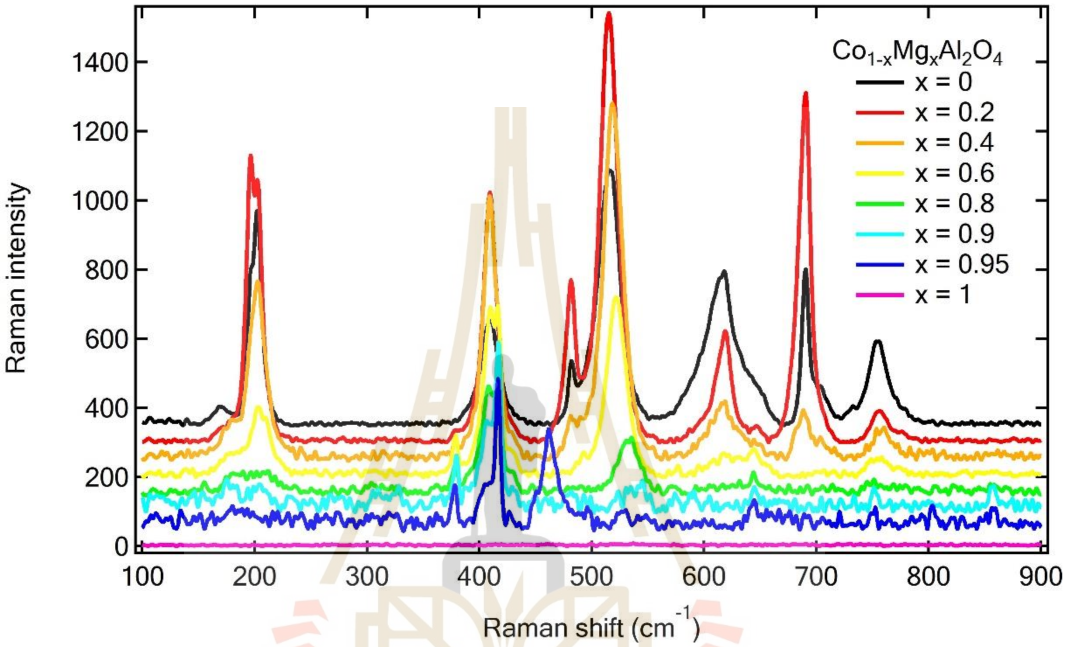

Figure 4.17 Raman spectra of $Co_{1-x}Mg_xAl_2O_4$ pigment calcined at 1200 °C with x equals to 0, 0.2, 0.4, 0.6, 0.8, 0.9, 0.95 and 1.0.

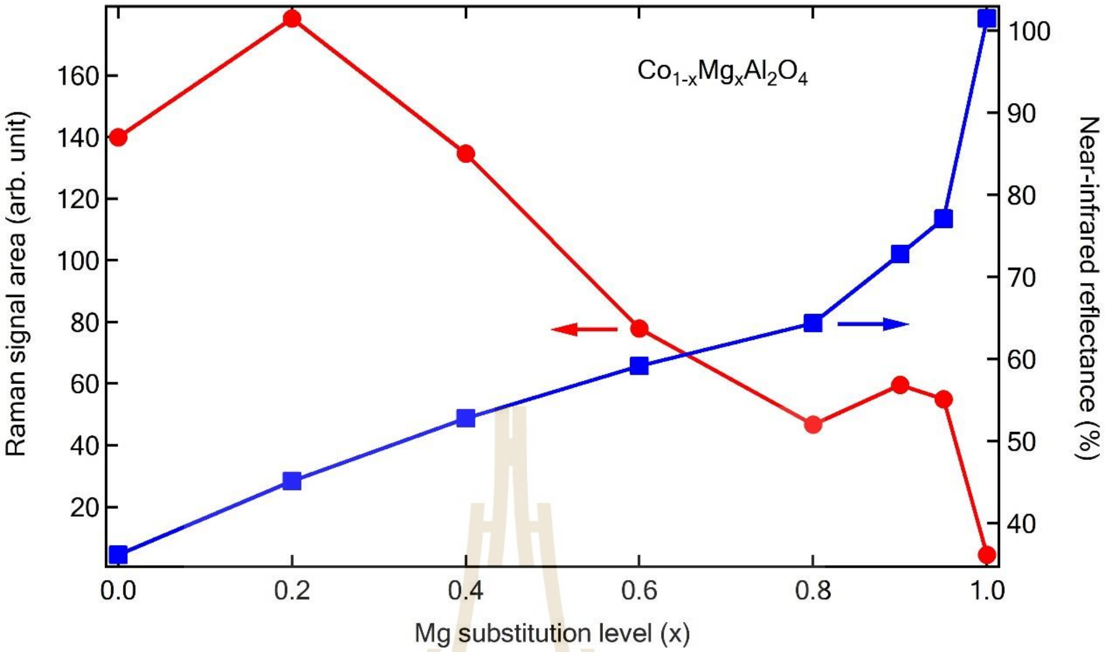

Figure 4.18 Raman signal area and near-infrared reflectance as a function of magnesium substitution level (x) in $Co_{1-x}Mg_xAl_2O_4$ system.

For the analysis of electronic properties using the valence band, we found that the conductivity of $Co_{1-x}Mg_xAl_2O_4$ blue pigment decreases when the magnesium substitution level are increased, indicated by the shift of valence band maximum (VBM) away from Fermi level shown in figure 4.19, which corresponds to the change of color of this pigment series, i.e., the color of pigment is brighter when increase the magnesium substitution level and eventually turns to white color for the $MgAl_2O_4$ end member as shown in figure 4.15. The brightening of pigment's color is a result of widening of bang gap which make the absorption of visible light decreased. Consequently, the reflectance of visible light increases.

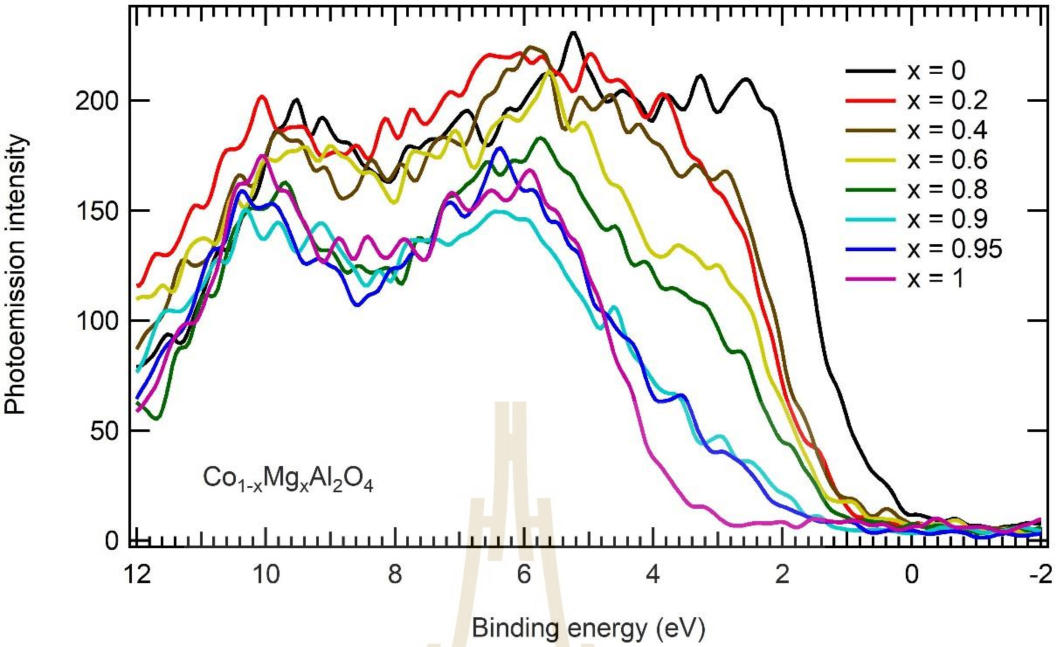

Figure 4.19 X-ray photoelectron spectra in valence band region of $Co_{1-x}Mg_xAl_2O_4$ pigment calcined at 1200 °C with x equals to 0, 0.2, 0.4, 0.6, 0.8, 0.9, 0.95 and 1.

By plotting the position of valence band maximum (VBM) and near-infrared reflectance percentage (%R) against the magnesium substitution level as shown in figure 4.20, the explicit positive correlation between both quantities was observed, i.e., when the VBM moves away from Fermi level, the metallicity of pigment tends to be lower which enhance the near-infrared reflectance as discussed above.

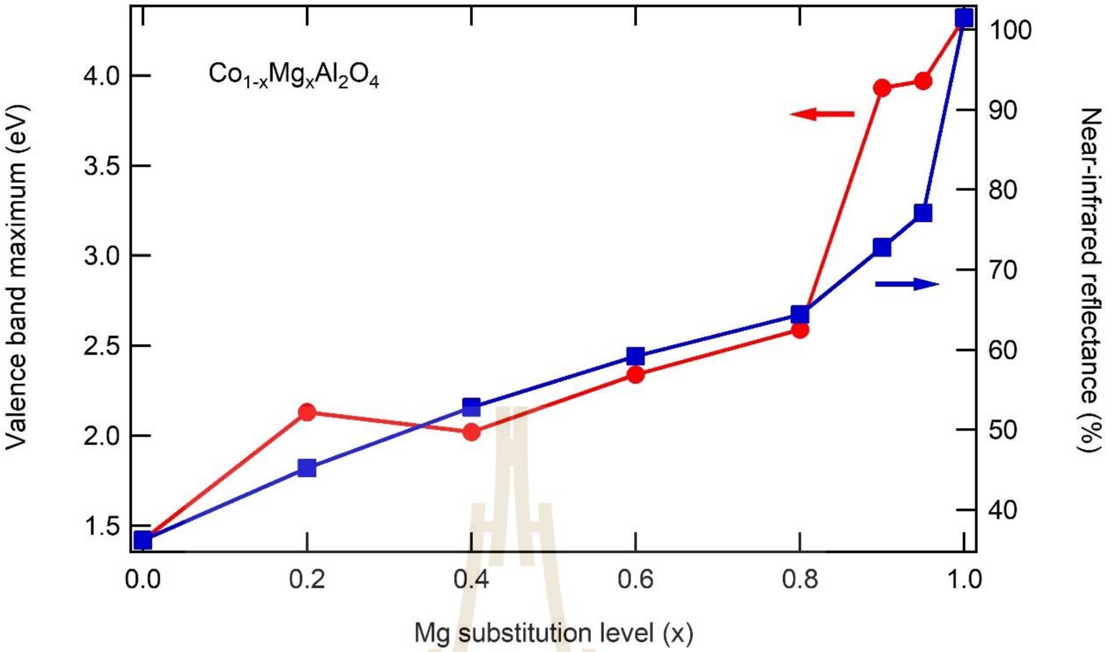

Figure 4.20 Valence band maximum (VBM) and near-infrared reflectance as a function of magnesium substitution level (x) in $Co_{1-x}Mg_xAl_2O_4$ system.

To confirm the change in electronic state, the Co 2*p* core level spectra were measured. Co 2*p* peaks, shown in figure 4.21, shifts to higher binding energy as x increasing from 0 to 0.6 which infer to the increasing of oxidation state of cobalt in $Co_{1-x}Mg_xAl_2O_4$ as magnesium content becomes larger.

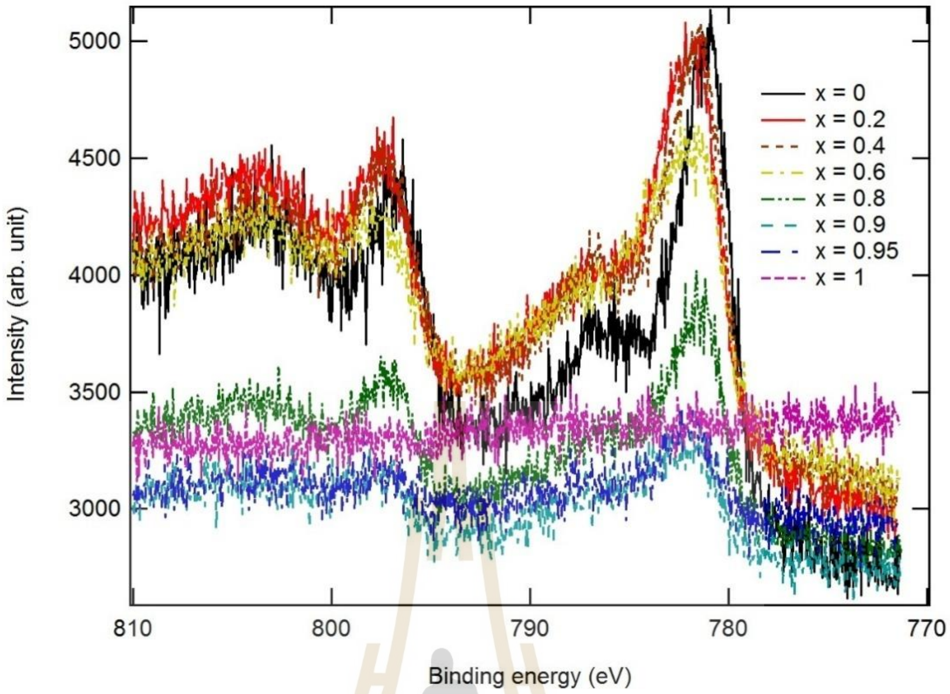

Figure 4.21 X-ray photoelectron spectra of $Co_{1-x}Mg_xAl_2O_4$ samples in cobalt (Co) core level region.

To evaluate the reproducibility of our approach, same pigment series were prepared and characterized separately in the same approach. Another $Co_{1-x}Mg_xAl_2O_4$ sample set, for the sake of reproducibility test, will be called $Co_{1-x}Mg_xAl_2O_4$ (II).

Raman spectra of $Co_{1-x}Mg_xAl_2O_4$ (II) pigment calcined at 1200 °C for 3 hours, shown in figure 4.22, indicate that $CoAl_2O_4$ exhibits higher number of vibration mode as well as higher Raman intensity than that of other pigments in this system. By comparing Raman signal area and near-infrared reflectance against the magnesium substitution level as shown in figure 4.23, we obviously found a strong negative correlation between these two quantities which is similar to that of the previous $Co_{1-x}Mg_xAl_2O_4$ (I) pigment set, shown in figure 4.18, as discussed before.

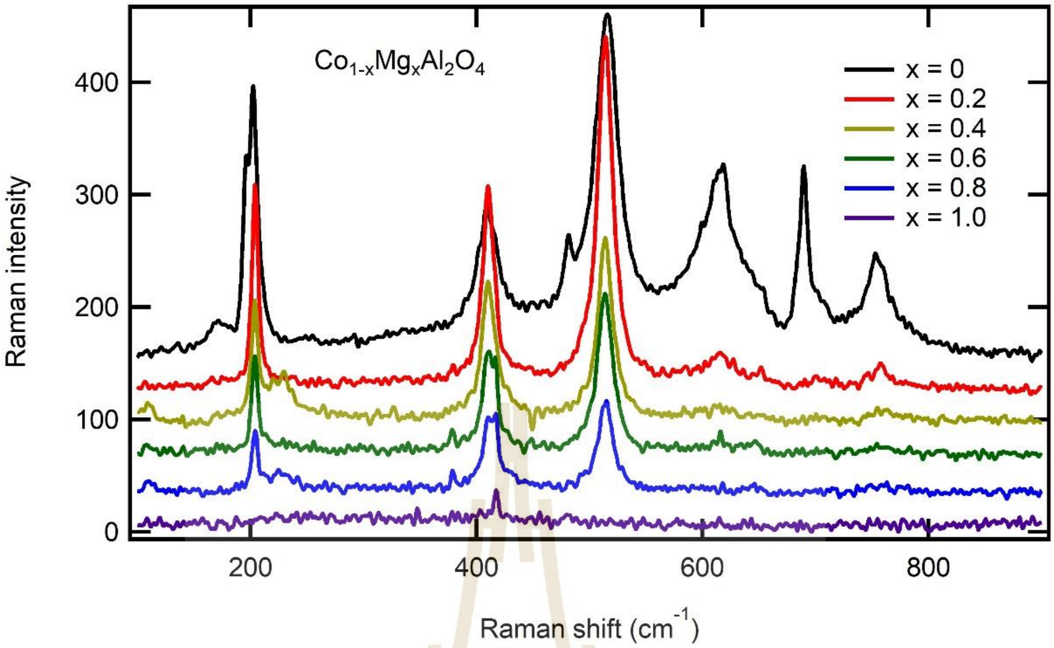

Figure 4.22 Raman spectra of $Co_{1-x}Mg_xAl_2O_4$ (II) pigment calcined at 1200 °C with x equals to 0, 0.2, 0.4, 0.6, 0.8 and 1.0.

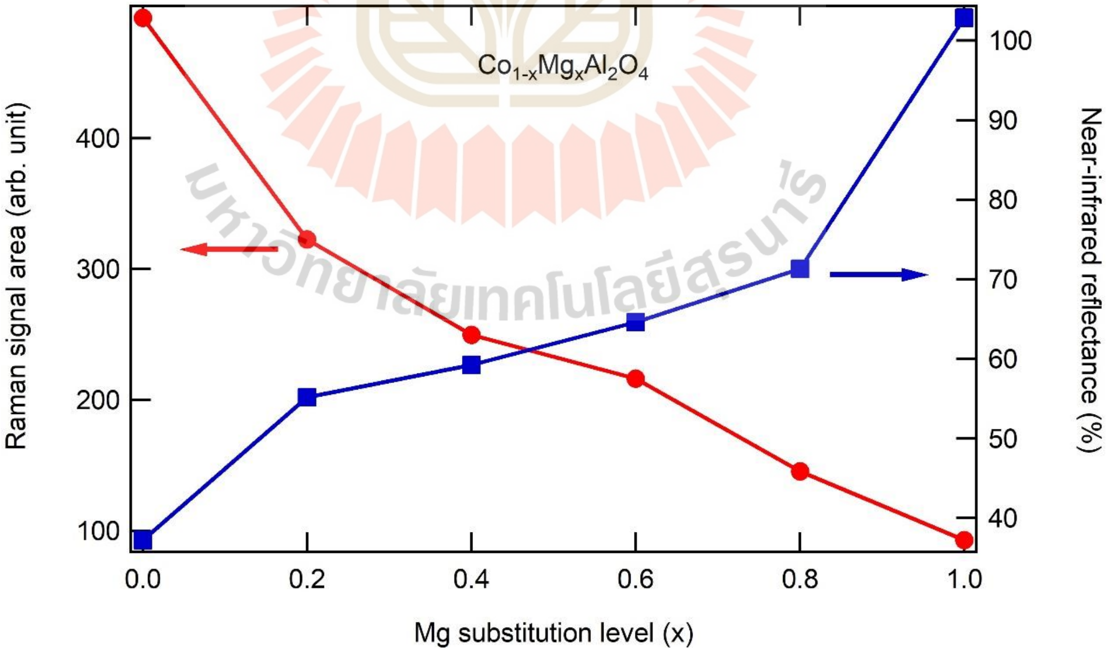

Figure 4.23 Raman signal area and near-infrared reflectance as a function of magnesium substitution level (x) in $Co_{1-x}Mg_xAl_2O_4$ (II) system.

Electronic property was also subjected to reproducibility test by using the same approach. By consider the valence band of $Co_{1-x}Mg_xAl_2O_4$ (II) system, shown in figure 4.24, we found that the band shifted away from Fermi level, infer to decreasing of conductivity and band gap widening, as magnesium content increased which is consistent with the color of pigment that brightened as magnesium concentration increased. By plotting valence band maximum and near-infrared reflectance against the magnesium substitution level as shown in figure 4.25, we, again, found the same trend as reported earlier in figure 4.20.

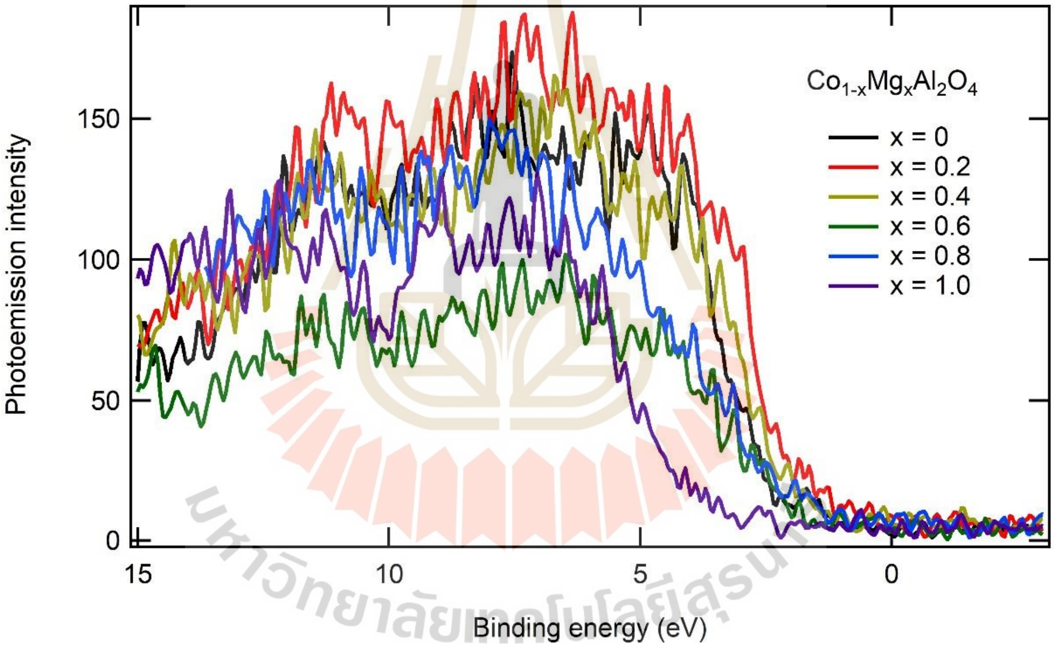

Figure 4.24 X-ray photoelectron spectra in valence band region of $Co_{1-x}Mg_xAl_2O_4$ (II) pigment calcined at 1200 °C with x equals to 0, 0.2, 0.4, 0.6, 0.8 and 1.

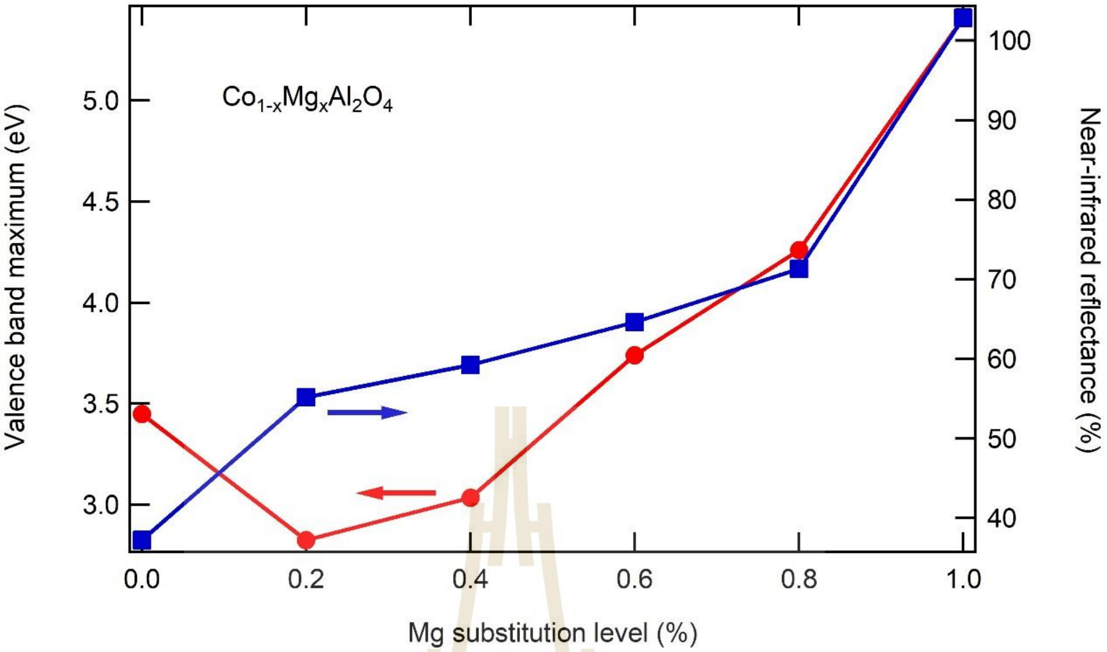

Figure 4.25 Valence band maximum (VBM) and near-infrared reflectance as a function of magnesium substitution level (x) in $Co_{1-x}Mg_xAl_2O_4$ (II) system.

The Co 2*p* spectra, shown in figure 4.26, also indicate the shifting of cobalt peaks to higher electron binding energy as magnesium content increased which refer to that the state of cobalt in $Co_{1-x}Mg_xAl_2O_4$ (II) system tend to change to higher oxidation state as substitution level increased.

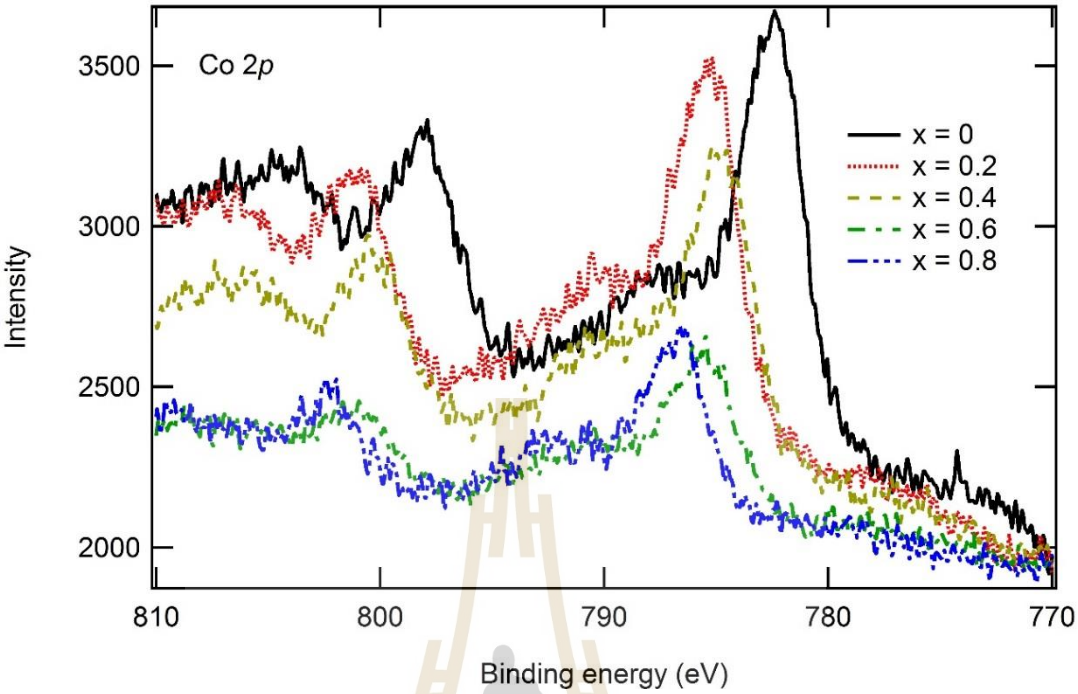

Figure 4.26 X-ray photoelectron spectra of $Co_{1-x}Mg_xAl_2O_4$ (II) samples in cobalt (Co) core level region.

In summary, the results from two blue pigment set, $Co_{1-x}Mg_xAl_2O_4$ (I) and $Co_{1-x}Mg_xAl_2O_4$ (II), confirm the reproducibility of the valence band maximum and Raman signal area evaluation. These pigment series exhibit strong correlation between electronic as well as phononic property and near-infrared reflectance.

4.3 $Zn_{1-x}Co_xFe_2O_4$ pigments

The color and appearance of as-prepared $Zn_{1-x}Co_xFe_2O_4$ pigments were shown in figure 4.27. As the cobalt content increased, the color of the pigment changes from dark yellow, for 0%Co substitution, to dark brown at 3.3% cobalt concentration. By reaching the highest substitution level conducted in this work, 30.1%Co, the pigment turns dark black. The intensity of pigment color is monotonically darkened by cobalt concentration.

Figure 4.27 $Zn_{1-x}Co_xFe_2O_4$ pigments calcined at 1100 °C with cobalt content ranged from 0 to 30.1 wt.%.

The XRD patterns of $Zn_{1-x}Co_xFe_2O_4$, shown in figure 4.28, obviously confirms phase change from $ZnFe_2O_4$, in unsubstituted sample, to mixed phase and finally leads to $CoFe_2O_4$-dominated structure at 23.4% and 30.1% substitution level.

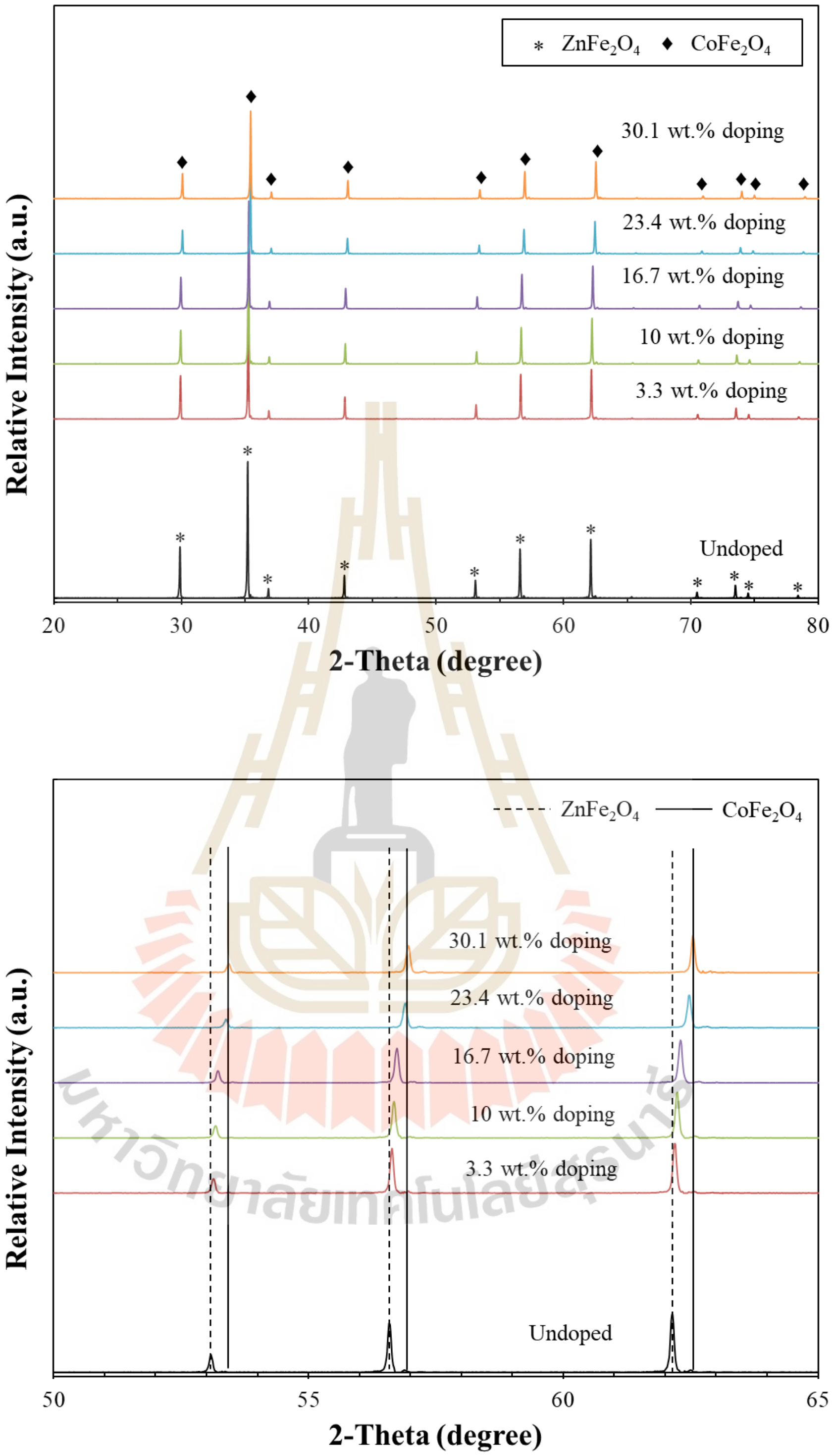

Figure 4.28 X-ray diffractogram of $Zn_{1-x}Co_xFe_2O_4$ pigments calcined at 1100 °C with cobalt content ranged from 0 to 30.1 wt.%.

Raman spectra of $Zn_{1-x}Co_xFe_2O_4$ pigments, shown in figure 4.29, revealed three main modes of vibration in Raman shift range of 100-800 cm^{-1}.

The relationship between Raman signal area (integrated over 100-800 cm^{-1} Raman shift range) and near-infrared reflectance of $Zn_{1-x}Co_xFe_2O_4$ pigments (shown in figure 4.30) indicates the inverse trend of these two quantities especially at small cobalt concentration. As cobalt content increased, near-infrared reflectivity is decreased with relatively small magnitude, and the Raman signal area also show similar trend. Up to 23.4% of cobalt concentration, the overall change of Raman signal area and near-infrared reflectance are in the opposite trend. However, the exception of the overall trend is observed in the for the last interval, from 23.4%Co to 30.1%Co point, in which the Raman signal area significantly drops to nearly the value of that of 0%Co and the trend for whole range of cobalt concentration could no longer be considered as a strong negative correlation.

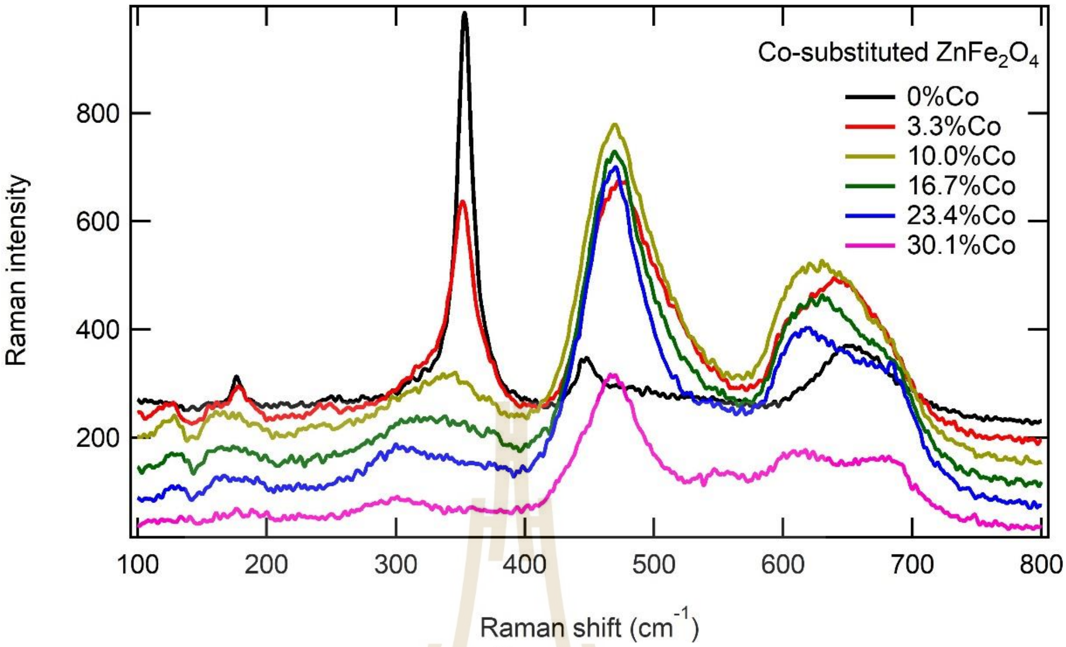

Figure 4.29 Raman spectra of $Zn_{1-x}Co_xFe_2O_4$ pigments with cobalt content ranged from 0 to 30.1 wt.%.

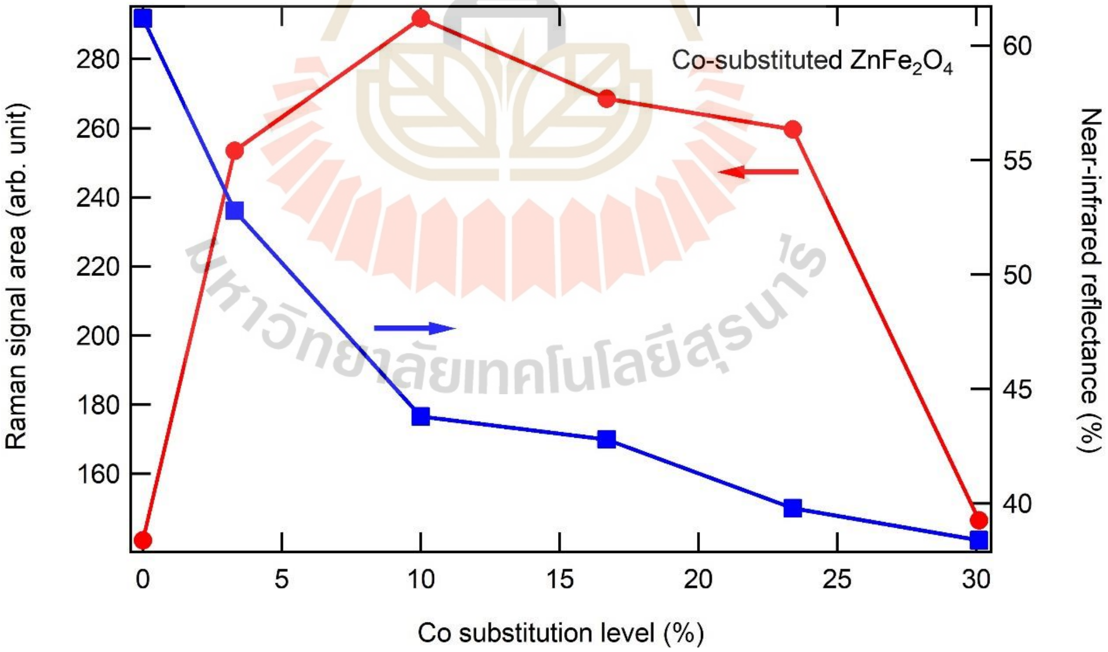

Figure 4.30 Raman signal area and near-infrared reflectance as a function of cobalt substitution level (x) in $Zn_{1-x}Co_xFe_2O_4$pigments.

Photoemission spectra of $Zn_{1-x}Co_xFe_2O_4$ pigments is shown in figure 4.31. In the big picture, valence band maximum tends to shift toward Fermi level as cobalt concentration in the structure is increased which is the characteristic of hole doping. This change is consistent with the introduction of cobalt into the parent structure which is the substitution of ZnO by Co_3O_4 precursor. The oxidation state from empirical formula of cobalt is +2 mixed with +3 while the value for ZnO is +2 which leads to substitution higher valent metal. Furthermore, the color intensity of pigment changes from dark yellow to black upon increasing cobalt concentration, which could indicate the band gap narrowing. All thing considered, the electronic state of $Zn_{1-x}Co_xFe_2O_4$ significantly changes in hole-doping fashion which underline the contribution of electron to near-infrared reflectivity in this pigment system.

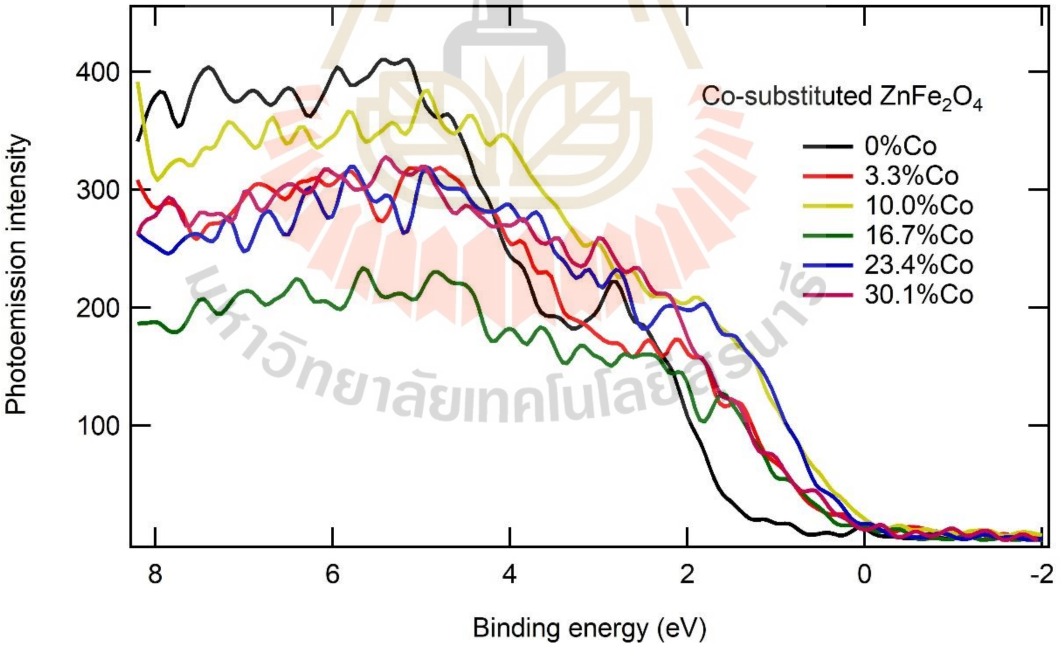

Figure 4.31 Photoemission spectra in valence band (VB) regime of $Zn_{1-x}Co_xFe_2O_4$ pigments with cobalt concentration in range of 0 – 30.1 wt.%.

By plotting valence band maximum (VBM) and near-infrared reflectance as a function of cobalt substitution level in $Zn_{1-x}Co_xFe_2O_4$ pigments, shown in figure 4.32, the decreasing trend of these two quantities are observed. As valence band shifts toward Fermi level, the conductivity of materials increased as well as the absorption of photon in visible and some part of near-infrared region tends to be increased. Therefore, the near-infrared reflectance of the pigment is likely to be higher which is consistent with our assumption.

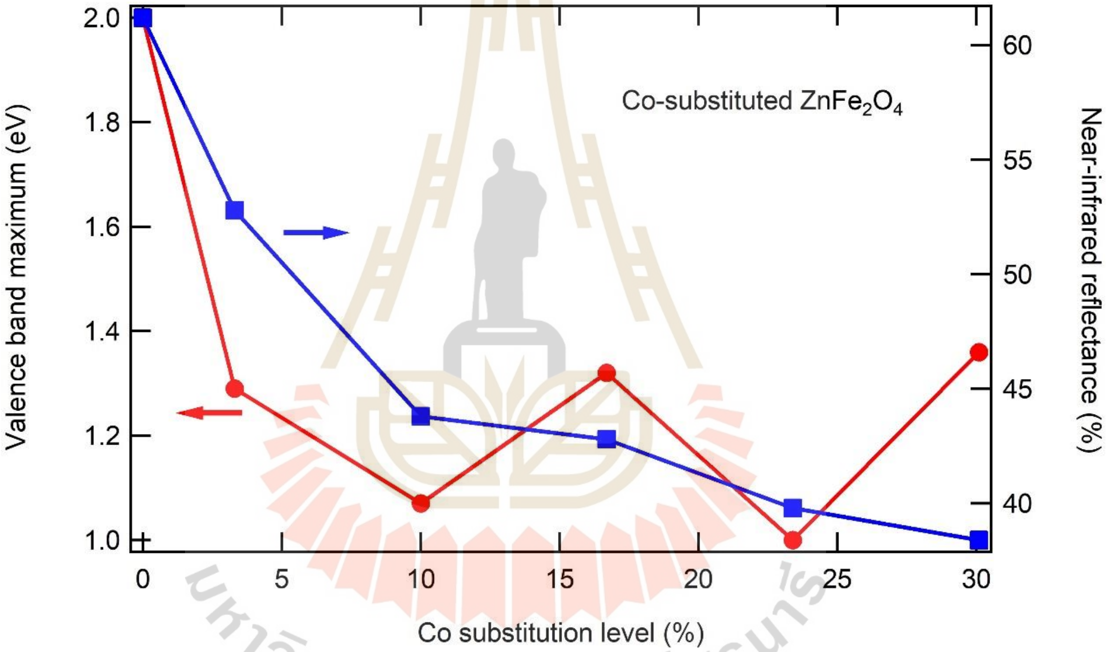

Figure 4.32 Valence band maximum (VBM) and near-infrared reflectance as a function of cobalt substitution level (x) in $Zn_{1-x}Co_xFe_2O_4$ pigments.

Core-level photoemission spectra of each metal component of $Zn_{1-x}Co_xFe_2O_4$ pigments indicate significant change in oxidation state of cobalt, zinc and iron (shown in figure 4.33, 4.34 and 4.35, respectively) as cobalt concentration in structure is increased which confirms the variation of electronic state upon substitution by heterovalent metal ion.

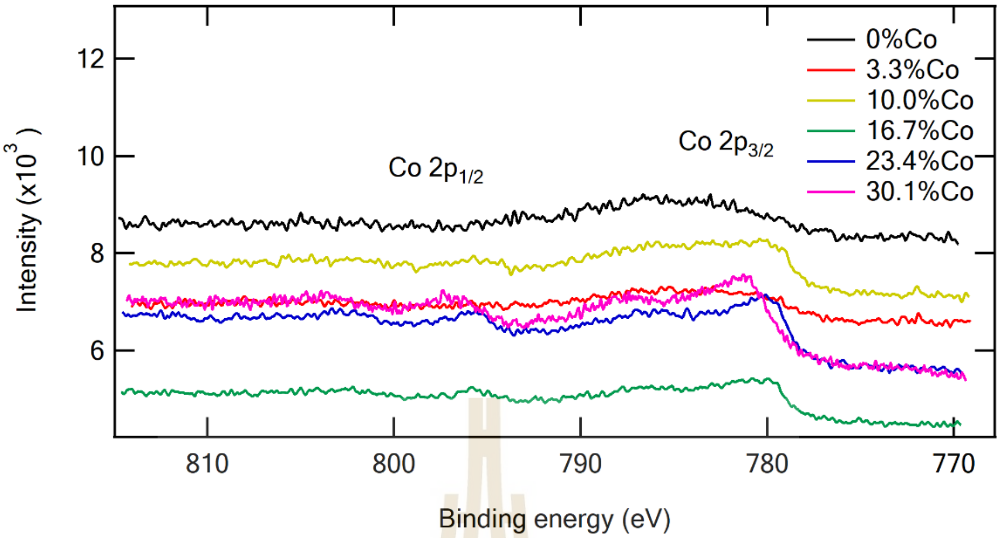

Figure 4.33 X-ray photoelectron spectrum in cobalt (Co) core level regime of $Zn_{1-x}Co_xFe_2O_4$ pigments with cobalt concentration in range of 0 – 30.1 wt.%.

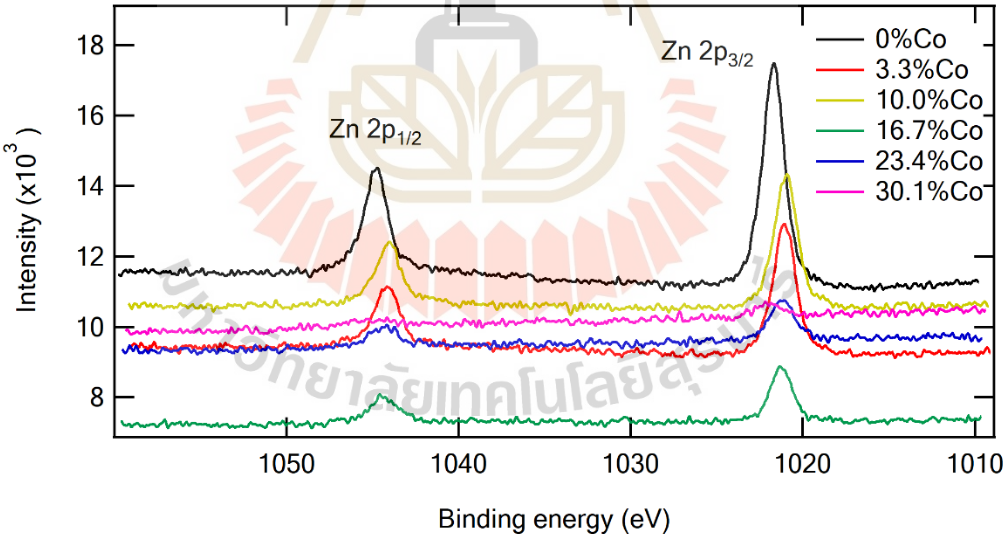

Figure 4.34 X-ray photoelectron spectrum in zinc (Zn) core level regime of $Zn_{1-x}Co_xFe_2O_4$ pigments with cobalt concentration in range of 0 – 30.1 wt.%.

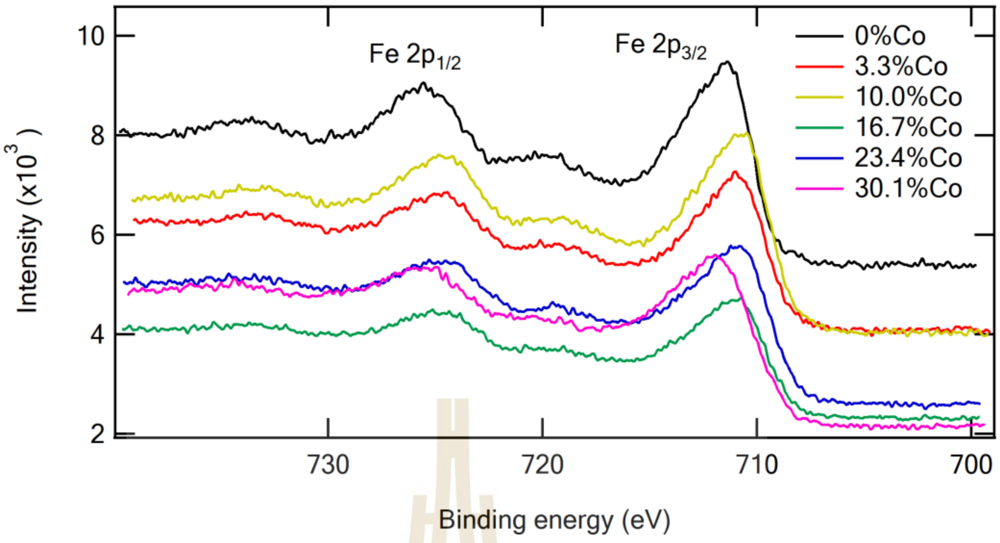

Figure 4.35 X-ray photoelectron spectrum in iron (Fe) core level regime of $Zn_{1-x}Co_xFe_2O_4$ pigments with cobalt concentration in range of 0 – 30.1 wt.%

4.4 $Cr_xSb_xTi_{1-2x}O_2$ pigments

For $Cr_xSb_xTi_{1-2x}O_2$ pigment calcined at 1200 °C, the parent structure is well-known titanium oxide white pigment. The increasing of chromium oxide and antimony oxide changes color of the resulting pigment to orange shade.

Valence bands of $Cr_xSb_xTi_{1-2x}O_2$ (shown in figure 4.36) reveal that TiO_2 parent structure is an insulator. When Cr_2O_3 and Sb_2O_3 are added and incorporated with TiO_2 in low content (small x value), the valence band shifts toward Fermi level which implies the higher electronic conductivity. However, when the content of Cr_2O_3 and Sb_2O_3 are further increased, at x value higher than 0.0125, the valence bands shift away from Fermi level which implies the lower electronic conductivity. As discussed before in previous pigment set, this change would indicate the role of electronic properties on pigment intensity and near-infrared reflectance of $Cr_xSb_xTi_{1-2x}O_2$

pigment. However, by considering the correlation coefficient which will be rigorously discussed in section 4.5, we found that the electronic state changes in this pigment series do not correlate to the change in near-infrared reflectance at all.

To obtain the detail in change titanium oxidation state as x increase, the Ti 2*p* core level photoemission spectra were measured (as shown in figure 4.38). The oxidation state of titanium is increased as x change from 0 to 0.0125 and continuously decreased as x is increased toward x = 0.3. We found that the trend in oxidation state/binding energy shifts over whole series is very similar to the change of valence band position as discussed previously. This similarity could imply that the change in valence band position of $Cr_xSb_xTi_{1-2x}O_2$ specifically corresponds to the change in oxidation state of titanium in the structure.

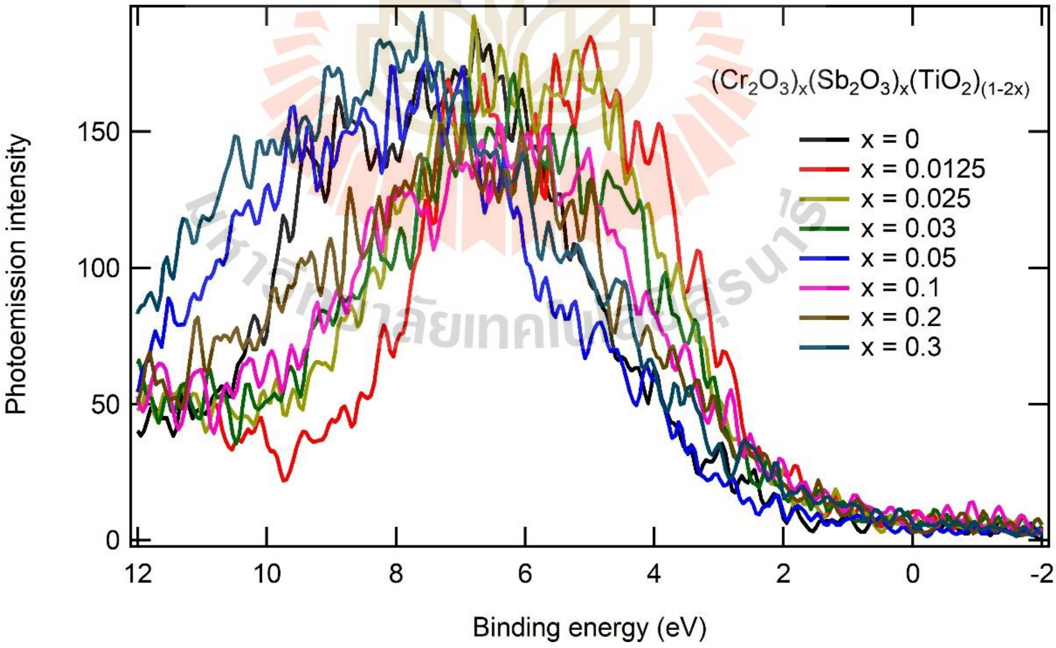

Figure 4.36 Photoemission spectra in valence band (VB) regime of $Cr_xSb_xTi_{1-2x}O_2$ pigments calcined at 1200 °C with x in range of 0 – 0.3.

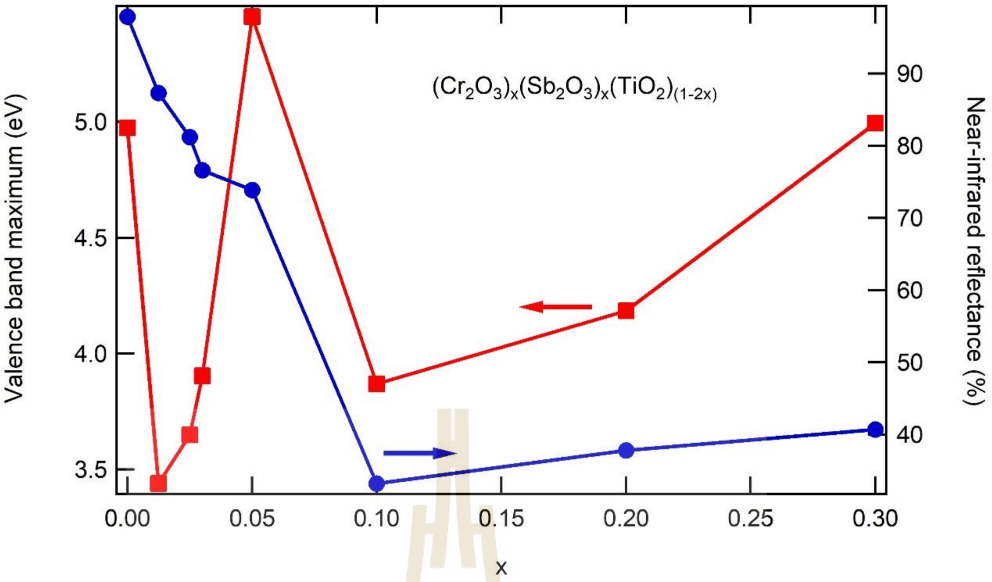

Figure 4.37 Valence band maximum (VBM) and near-infrared reflectance as a function of x in $Cr_xSb_xTi_{1-2x}O_2$ pigments.

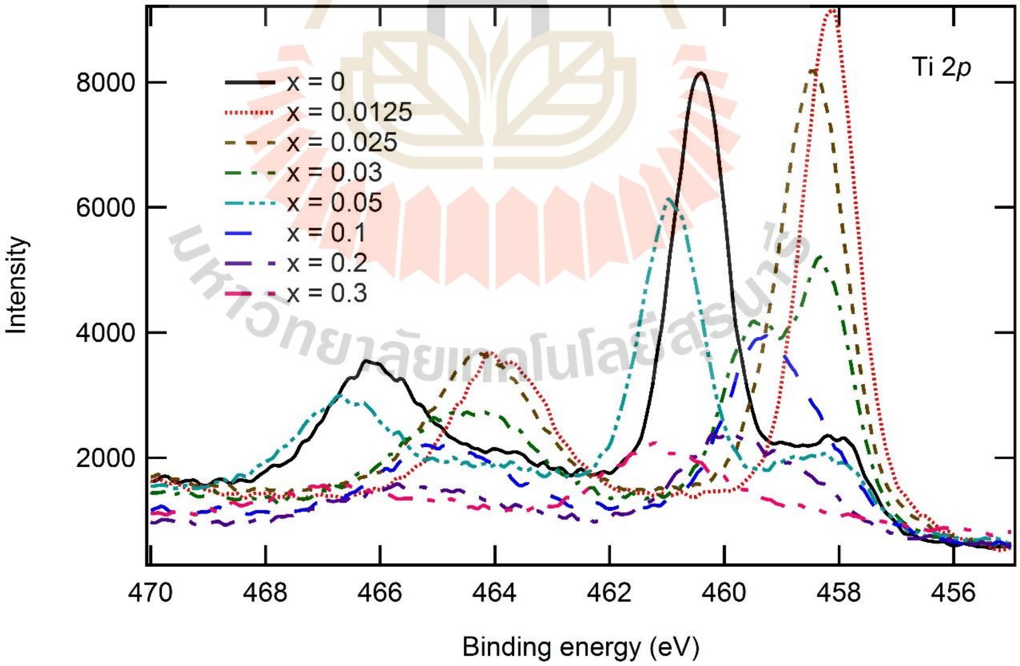

Figure 4.38 X-ray photoelectron spectrum in titanium (Ti) core level regime of $Cr_xSb_xTi_{1-2x}O_2$ pigments calcined at 1200 °C with x in range of 0 – 0.3.

Raman spectra intensity of $Cr_xSb_xTi_{1-2x}O_2$ are monotonically decreased as TiO_2 composition is decreased (shown in figure 4.39) which is in the same trend as the change in near-infrared reflectance of $Cr_xSb_xTi_{1-2x}O_2$ (shown in figure 4.40). However, this correlation contradicts with the assumption proposed earlier. As state in the discussion of the correlation between phononic absorption and near-infrared reflectance of pigment for previous three pigment series, the area under Raman spectra signal correspond to phononic absorption of pigment. Consequently, high Raman intensity signal indicates that phononic absorption significantly contribute to near-infrared reflectivity. Nevertheless, for $Cr_xSb_xTi_{1-2x}O_2$, this explanation is invalid due to that the direction of change is opposite to the assumption. To explain this exception, we found that this result might related to the very high, approximately 98%, near-infrared reflectance of TiO_2 parent structure which almost reaches 100% reflectance. Therefore, the margin of improving the near-infrared reflectance is limited by the very high reflectance of parent structure which leading to either nonresponse or decreasing of near-infrared reflectance as added components increased.

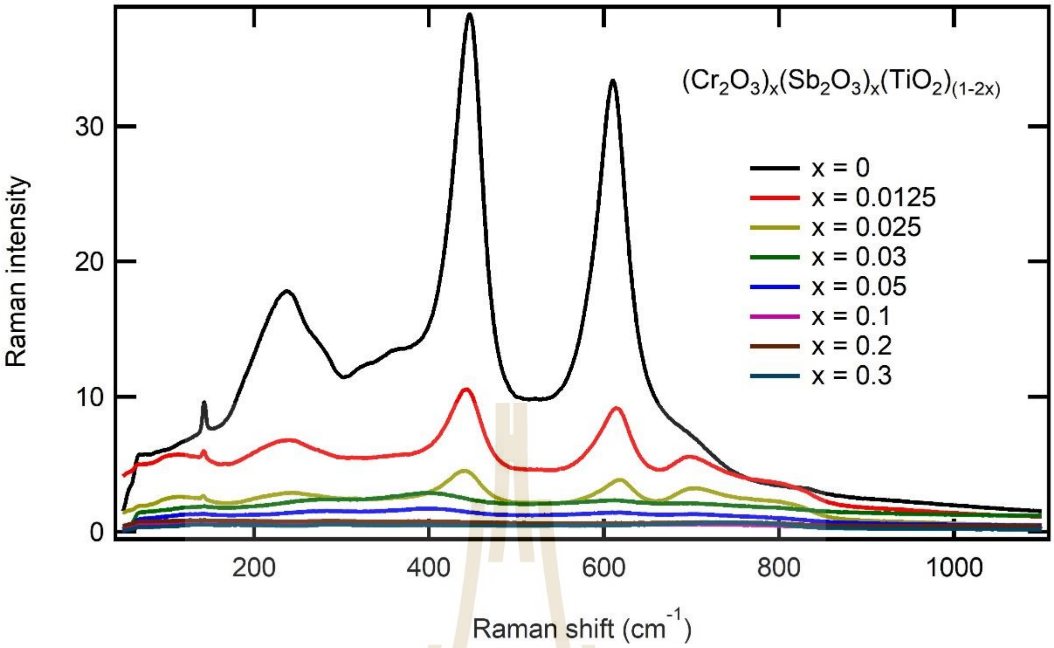

Figure 4.39 Raman spectra of $Cr_xSb_xTi_{1-2x}O_2$ pigments calcined at 1200 °C with x in range of 0 – 0.3.

The decreasing of phononic absorption contribution with the lower of near-infrared reflectance can be explained by the presence of damped vibration. By introducing Cr_2O_3 and Sb_2O_3 to TiO_2 parent structure, new mode of lattice vibration would also be introduced to the whole system. The newly added vibrational modes could suppress the overall vibration via destructive interference with the existing modes, thus leads to the damped vibration character which significantly reduce the vibration amplitude. Eventually, the absorption by lattice vibration of the system would decrease.

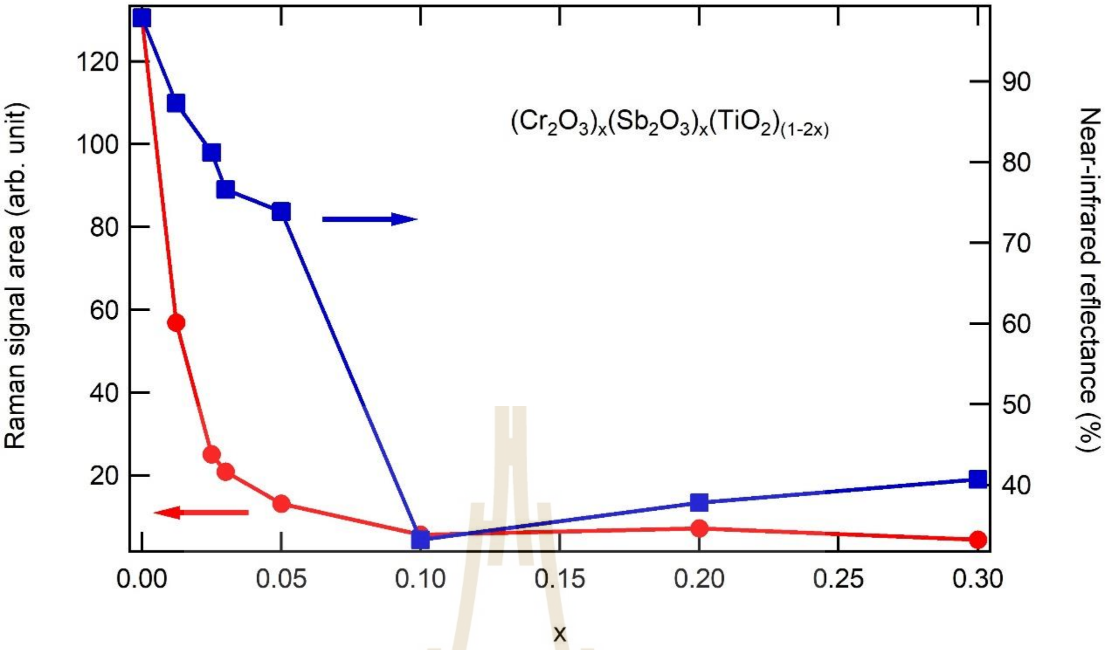

Figure 4.40 Raman signal area and near-infrared reflectance as a function of x in $Cr_xSb_xTi_{1-2x}O_2$ pigments calcined at 1200 °C.

4.5 Correlation between electronic/phononic behavior and near-infrared reflectance of oxide pigments

In the final part of this chapter, the data related to electronic/phononic behavior and near infrared reflectance of every pigment set studied in this work are analyzed and summarized by means of statistical correlation.

The Pearson product-moment correlation coefficients indicate the correlation between Raman signal area (phononic behavior) and near-infrared reflectance as well as valence band maximum (electronic behavior) and near-infrared reflectance are shown in table 4.1.

Table 4.1 Pearson product-moment correlation coefficient of various pigment showing the correlation between valence band maximum (VBM) and near-infrared reflectance as well as Raman signal area (RSA) and near-infrared reflectance.

	VBM - NIR reflectance	RSA – NIR reflectance
Ti-sub Cr-Fe oxide	0.59	-0.16
$Co_{1-x}Mg_xAl_2O_4$ (I)	0.93	-0.84
$Co_{1-x}Mg_xAl_2O_4$ (II)	0.85	-0.91
$Zn_{1-x}Co_xFe_2O_4$	0.79	-0.34
$Cr_xSb_xTi_{1-2x}O_2$	N/A	0.74

In summary, the anticipated correlation coefficient of valence band maximum and near-infrared reflectance is positive while the anticipated correlation coefficient of Raman signal area and near-infrared reflectance is negative as the assumption proposed earlier. Three out of five pigment, *i.e.*, $Co_{1-x}Mg_xAl_2O_4$ (I), $Co_{1-x}Mg_xAl_2O_4$ (II) and $Zn_{1-x}Co_xFe_2O_4$ show a strong positive correlation between electronic properties and near-infrared reflectance by exhibit the coefficient greater than 0.70. The same three series also show a strong negative correlation between phononic properties and near-infrared reflectance by exhibit the coefficient lower than -0.70 (also true for cobalt-substituted $ZnFe_2O_4$ in case the outlier is omitted).

For $Cr_xSb_xTi_{1-2x}O_2$, electronic contribution plays no role in this pigment series while the phonon correlates with near-infrared in the opposite fashion as we proposed.

The unexpected correlation coefficient value was found in the titanium-substituted chromium iron oxide pigment series. In the section 4.2, at first, we have interpreted the resulted as electronic behavior play no role to near-infrared reflectance. However, the correlation coefficient calculation shows the moderate positive correlation between electronic behavior and near-infrared reflectance. This discrepancy could be explained by the very small magnitude of change in valence band maximum observed from bare graph which are likely to be unchanged, shown in figure 4.7, leads to the primary summary as the non-correlative result. Nevertheless, the correlation coefficient calculation is not affected by changing magnitude. The changing direction is more important in correlation coefficient calculation. This can be used for another discrepancy found in primary summary, section 4.2, on phononic properties and near-infrared reflectance. The result was firstly interpreted as the negative correlation between phononic behavior and near-infrared reflectance. However, the correlation coefficient points out that these two properties show very weak negative correlation to each other with the coefficient of -0.16.

From the knowledge gained from correlation between electronic/phononic absorption and near-infrared reflectance of oxide pigments, we can make a general suggestion on the development of near-infrared reflective pigment. In case we start with an insulator parent structure with very high near-infrared reflectance, *e.g.*, white Al_2O_3 and TiO_2 pigments which are good examples of band insulator, in order to maintain a high reflectance while tuning the color appearance, we need to dope the parent structure in the way that decrease the crystal structure quality, *e.g.*, decreasing the particle size, to suppress the absorption by lattice vibration. Another strategy for tuning phonic absorption without significantly changing the electronic structure is to dope the parent structure with the element which is in the same column but different row in periodic table. By using this approach, the atomic mass of dopant is different from the one originally sits in the parent structure which will alter the lattice vibration while the oxidation state of dopant tends to be similar to the substituent element especially for main group element. From electronic absorption viewpoint, we can dope the parent structure in electron doping fashion to decrease the absorption by electron due to the shifting of valence band away from Fermi level as discussed in detail previously.

CHAPTER V

CONCLUSION

Four ceramic pigment series were successfully prepared by solid state reaction method with structural confirmation by x-ray diffraction. The obtained pigments were then subjected to the near-infrared reflectance measurement to observe the potential of each pigment to be applied in solar-reflective paint industry. The research objectives of this work are finding the factor governed the pigment's solar-reflective ability in near-infrared regime and quantification of each factor affected the near-infrared reflectance.

At first, we started with the basic assumption that there are two basic contribution that influence the ability to reflect near-infrared radiation in oxide pigment, *i.e.*, electronic and phononic contribution. On one step further, the electronic and absorption on solar radiation of pigment would inversely be proportional to near-infrared reflectance which is straightforward in case transmittance is negligible like what are happened in our pigments.

X-ray photoemission spectroscopy and Raman spectroscopy are employed for electronic and phononic absorption investigation in oxide pigments, respectively. On electronic view, in general picture, the bigger the electronic band gap, the smaller the ability to absorb the incident photon which would enhance the near-infrared reflectance. On the phononic view, the lower number and strength of vibrational mode, the smaller lattice absorption and non-radiative process which would also enhance the near-infrared reflectance. From the assumption, near-infrared reflectance would be directly proportional to energy band gap, or valence band maximum measured relative to Fermi level. Whereas near-infrared reflectance would inversely be proportional to integrated Raman signal area. In other word, we could say that near-infrared would show positive correlation with valence band maximum position and negative correlation with Raman signal area.

From the experiment, three out of four pigment series exhibit positive correlation between near-infrared reflectance and valence band maximum (electronic properties) while the exception was found in titanium-substituted chromium iron oxide pigment series which shows non-correlative result between these quantities. In phononic consideration, the same three out of four pigment series exhibit negative correlation between near-infrared reflectance and Raman signal area as we expected from the assumption while the $Cr_xSb_xTi_{1-2x}O_2$ pigment series shows the opposite correlation sign which could pave the way to the compromission between near-infrared reflection and dark color tuning.

REFERENCES

REFERENCES

Baneshi, M., Gonome, H., and Maruyama, S. (2016). Cool black roof impacts into the cooling and heating load demand of a residential building in various climates. **Solar Energy Materials and Solar Cells**. 152: 21-33.

Bittler, K., and Ostertag, W. (1980). Developments in the Field of Inorganic Pigments. **Angewandte Chemie.** 19: 190-196.

Cornell, R. M., and Schwertmann, U. (2003) The Iron Oxides: Structure, Properties, Reactions, Occurrences and Uses. 2nd Edition, **Wiley-VCH**.

Einstein, A. (1905). Über einen die Erzeugung und Verwandlung des Lichtes betreffenden heuristischen Gesichtspunkt. **Annalen der Physik.** 322: 132-148.

Harroun, S. G., Bergman, J., Jablonski, E., and Brosseau, C. L. (2011). Surface-enhanced Raman spectroscopy analysis of house paint and wallpaper samples from an 18th century historic property. **Analyst**. 136(17): 3453-3460.

Hertz, H. (1887). Ueber einen Einfluss des ultravioletten Lichtes auf die electrische Entladung. **Annalen der Physik.** 267: 983-1000.

Hund, F. (1981). Inorganic Pigments: Bases for Colored, Uncolored, and Transparent Products. **Angewandte Chemie.** 20: 723-730.

Jansen, M., and Letschert, H. P. (2000). Inorganic yellow-red pigments without toxic metals. **Nature.** 404(6781): 980-982.

Kaur, B., Quazi, N., Ivanov, I., and Bhattacharya, S. N. (2012). Near-infrared reflective properties of perylene derivatives. **Dyes and Pigments**. 92(3): 1108-

1113.

Kumari, L. S., Rao, P. P., Radhakrishnan, A. N. P., James, V., Sameera, S., and Koshy, P. (2013). Brilliant yellow color and enhanced NIR reflectance of monoclinic $BiVO_4$ through distortion in VO_4^{3-} tetrahedra. **Solar Energy Materials and Solar Cells**. 112: 134-143.

Kumari, L. S., Rao, P. P., Radhakrishnan, A. N. P., James, V., Sameera, S., and Koshy, P. (2013). Brilliant yellow color and enhanced NIR reflectance of monoclinic $BiVO_4$ through distortion in VO_4^{3-} tetrahedra. **Solar Energy Materials and Solar Cells.** 112: 134-143.

Levinson, R., Berdahl, P., Akbari, H., Miller, W., Joedicke, I., Reilly, J., Suzuki, Y., and Vondran, M. (2007). Methods of creating solar-reflective nonwhite surfaces and their application to residential roofing materials. **Solar Energy Materials and Solar Cells**. 91(4): 304-314.

Levinson, R., Akbari, H., and Berdahl, P. (2010). Measuring solar reflectance-Part I: Defining a metric that accurately predicts solar heat gain. **Solar Energy**. 84(9): 1717-1744.

Liang, S.-T., Zhang, H.-L., Luo, M.-T., Liu, H.-X., Bai, Y.-L., Xu, H.-B., and Zhang, Y. (2015). Preparation of Cr_2O_3-based pigments with high NIR reflectance via thermal decomposition of CrOOH. **Transactions of Nonferrous Metals Society of China.** 25: 2646-2647.

Malshe, V. C., and Bendiganavale, A. K. (2008). Infrared reflective inorganic pigments. **Recent Patents on Chemical Engineering**. 1(1): 67-79.

Nordling, C., Sokolowski, E., and Siegbahn, K. (1957). Precision Method for Obtaining Absolute Values of Atomic Binding Energies. **Physical Review.**

105: 1676-1677.

Orna, M. V. (2015). Historic mineral pigments: Colorful benchmarks of ancient civilizations. **ACS Symposium Series.** 1211: 17-69.

Plendl, J. N. (1971). Damping of Lattice Vibrations in Solids. **Applied Optics.** 10: 87-97.

Qing, X., Yuan, L., Wang, C., Bi, M., Wang, Y., and Weng, X. (2020). Structural and visible-near infrared optical properties of (Fe, Mo)-co-doped TiO_2 for colored cool pigments. **Journal of Alloys and Compounds.** 826: 153946.

Raj, A. K. V., Prabhakar Rao, P., Divya, S., and Ajuthara, T. R. (2017). Terbium doped Sr_2MO_4 [M = Sn and Zr] yellow pigments with high infrared reflectance for energy saving applications. **Powder Technology**. 311: 52-58.

Roberts, A. J., and Moffitt, C. E. (2019). Trends in XPS instrumentation for industrial surface analysis and materials characterization. **Journal of Electron Spectroscopy and Related Phenomena**. 231: 68-74.

Santamouris, M., Pavlou, K., Synnefa, A., Niachou, K., and Kolokotsa, D. (2007). Recent progress on passive cooling techniques. Advanced technological developments to improve survivability levels in low-income households. **Energy and Buildings**. 39: 859-866.

Santamouris, M., Synnefa, A., and Karlessi, T. (2011). Using advanced cool materials in the urban built environment to mitigate heat islands and improve thermal comfort conditions. **Solar Energy**. 85(12): 3085-3102.

Synnefa, A., Santamouris, M., and Akbari, H. (2007). Estimating the effect of using cool coatings on energy loads and thermal comfort in residential buildings in various climatic conditions. **Energy Build.** 39: 1167-1174.

Taffa, D. H., Dillert, R., Ulpe, A. C., Bauerfeind, K. C. L., Bredow, T., Bahnemann, D. W., and Wark, M. (2017). Photoelectrochemical and theoretical investigations of spinel type ferrites ($MxFe_{3-x}O_4$) for water splitting: A mini-review. **Journal of Photonics for Energy.** 7: 012009.

Takebayashi, H., and Moriyama, M. (2007). Surface heat budget on green roof and high reflection roof for mitigation of urban heat island. **Building and Environment**. 42(8): 2971-2979.

van Driel, B. A., Kooyman, P. J., van den Berg, K. J., Schmidt-Ott, A., and Dik, J. (2016). A quick assessment of the photocatalytic activity of TiO2 pigments - From lab to conservation studio!. **Microchemical Journal.** 126: 162-171.

Voss, L., Hsiao, I. L., Ebisch, M., Vidmar, J., Dreiack, N., Böhmert, L., Stock, V., Braeuning, A., Loeschner, K., Laux, P., Thünemann, A. F., Lampen, A., and Sieg, H. (2020). The presence of iron oxide nanoparticles in the food pigment E172. **Food Chemistry.** 327: 127000.

Vishnu, V. S., and Reddy, M. L. (2011). Near-infrared reflecting inorganic pigments based on molybdenum and praseodymium doped yttrium cerate: Synthesis, characterization and optical properties. **Solar Energy Materials and Solar Cells**. 95: 2685-2692.

Yuan, L., Han, A., Ye, M., Chen, X., Yao, L., and Ding, C. (2018). Synthesis and characterization of environmentally benign inorganic pigments with high NIR reflectance: Lanthanum-doped $BiFeO_3$. **Dyes and Pigments**. 148: 137-146.

Zou, J., Zhang, P., Liu, C., and Peng, Y. (2014). Highly dispersed (Cr, Sb)-co-doped rutile pigments of cool color with high near-infrared reflectance. **Dyes and Pigments.** 109: 113-119.

CURRICULUM VITAE

Name	Mr. Worasarit Saengsui
Date of Birth	November 18th, 1987
Place of Birth	Uthaithani, Thailand
E-mail	worasarit.s@gmail.com

Education

2006-2010	B.S. (Chemistry), Kasetsart University, Thailand
2010-2013	M.S. (Nanomaterials Science), Kasetsart University, Thailand
2016-present	Ph.D. (Physics), Suranaree University of Technology, Thailand